

The P.N.S Elliptical Galaxy Survey: a standard Λ CDM halo around NGC 4374?^{*}

N.R. Napolitano^{1†}, A.J. Romanowsky^{2,3}, M. Capaccioli^{4,5}, N.G. Douglas⁶,
M. Arnaboldi^{7,8}, L. Coccato⁹, O. Gerhard⁹, K. Kuijken¹⁰, M.R. Merrifield¹¹,
S.P. Bamford¹¹, A. Cortesi¹¹, P. Das⁹, K.C. Freeman¹²

¹ *INAF-Observatory of Capodimonte, Salita Moiarriello, 16, 80131, Naples, Italy*

² *UCO/Lick Observatory, University of California, Santa Cruz, CA 95064, USA*

³ *Departamento de Física, Universidad de Concepción, Casilla 160-C, Concepción, Chile*

⁴ *Dipartimento di Scienze Fisiche, Università Federico II, Via Cinthia, 80126, Naples, Italy*

⁵ *MECENAS, University of Naples Federico II and University of Bari, Italy*

⁶ *Kapteyn Astronomical Institute, Postbus 800, 9700 AV Groningen, The Netherlands*

⁷ *European Southern Observatory, Karl-Schwarzschild-Strasse 2, D-85748 Garching, Germany*

⁸ *INAF, Osservatorio Astronomico di Pino Torinese, I-10025 Pino Torinese, Italy*

⁹ *Max-Planck-Institut für Extraterrestrische Physik, Giessenbachstrasse, D-85748 Garching b. München, Germany*

¹⁰ *Leiden Observatory, Leiden University, PO Box 9513, 2300RA Leiden, The Netherlands*

¹¹ *School of Physics and Astronomy, University of Nottingham, University Park, Nottingham NG7 2RD, UK*

¹² *Research School of Astronomy & Astrophysics, ANU, Canberra, Australia*

Accepted 2010 October 07. Received 2010 October 06; in original form 2010 September 16

ABSTRACT

As part of our current programme to test Λ CDM predictions for dark matter (DM) haloes using extended kinematical observations of early-type galaxies, we present a dynamical analysis of the bright elliptical galaxy NGC 4374 (M84) based on ~ 450 Planetary Nebulae (PNe) velocities from the PN.Spectrograph, along with extended long-slit stellar kinematics.

This is the first such analysis of a galaxy from our survey with a radially constant velocity dispersion profile. We find that the spatial and kinematical distributions of the PNe agree with the field stars in the region of overlap.

The velocity kurtosis is consistent with zero at almost all radii.

We construct a series of Jeans models, fitting both velocity dispersion and kurtosis to help break the mass-anisotropy degeneracy. Our mass models include DM halos either with shallow cores or with central cusps as predicted by cosmological simulations – along with the novel introduction in this context of adiabatic halo contraction from baryon infall.

Both classes of models confirm a very massive dark halo around NGC 4374, demonstrating that PN kinematics data are well able to detect such haloes when present. Considering the default cosmological mass model, we confirm earlier suggestions that bright galaxies tend to have halo concentrations higher than Λ CDM predictions, but this is found to be solved if either a Salpeter IMF or adiabatic contraction with a Kroupa IMF is assumed. Thus for the first time a case is found where the PN dynamics may well be consistent with a standard dark matter halo. A cored halo can also fit the data, and prefers a stellar mass consistent with a Salpeter IMF. The less dramatic dark matter content found in lower-luminosity “ordinary” ellipticals suggests a bimodality in the halo properties which may be produced by divergent baryonic effects during their assembly histories.

Key words: galaxies: elliptical — galaxies: kinematics and dynamics — galaxies: structure — galaxies: individual: NGC 4374 — dark matter — planetary nebulae: general

1 INTRODUCTION

The standard cosmological model, the so-called Λ CDM (cold dark matter with a cosmological constant; see e.g. Hinshaw et al. 2009), has been challenged by kinematical measurements of dwarf and spiral galaxies (Gentile et al. 2005; McGaugh et al. 2007; Gilmore et al. 2007; Salucci et al. 2007; Spano et al. 2008; Kuzio de Naray et al. 2008; but see e.g. Johansson et al. 2009; Governato et al. 2010). The confrontation of the predictions of the Λ CDM with early-type galaxies (ETGs hereafter) is instead more uncertain. On the one hand, X-rays (see Paolillo et al. 2003; O’Sullivan & Ponman 2004b; Humphrey et al. 2006; Johnson et al. 2009; Das et al. 2010) or discrete tracers such as globular clusters (e.g. Romanowsky et al. 2009; Shen & Gebhardt 2010; Schuberth et al. 2010; Woodley et al. 2010) confirmed the presence of massive haloes in the most luminous systems, particularly at the centres of groups and clusters. On the other hand, ordinary ETGs, probed with planetary nebulae (PNe), have manifested discrepancies with Λ CDM expectations (see e.g. Romanowsky et al. 2003, hereafter R+03; Napolitano et al. 2005, hereafter N+05) which may be real or due to the limitations of observations and dynamical analysis.

ETGs are difficult to probe with standard kinematical techniques (Paolillo et al. 2003; O’Sullivan & Ponman 2004a; Pellegrini & Ciotti 2006; Bergond et al. 2006; Pellegrini et al. 2007), while they are within the reach of the Planetary Nebula Spectrograph (PN.S; Douglas et al. 2002) which along with other instruments is producing large kinematical samples of PNe in a variety of galaxy types (R+03; Peng et al. 2004; Merrett et al. 2006; Douglas et al. 2007, hereafter D+07; Noordermeer et al. 2008; Méndez et al. 2009; Napolitano et al. 2009, hereafter N+09; Coccato et al. 2009, hereafter C+09; Herrmann & Ciardullo 2009; Teodorescu et al. 2010).

One of the main findings emerging from these observations is the bimodal behavior of ETG velocity dispersion profiles in the outer regions: steeply falling and roughly constant (Napolitano et al. 2008; C+09). These profiles seem to generally (but not perfectly) track the bimodality of the central regions of ETGs, which fall into the two classes of disk, fast rotators of “ordinary” luminosity, and boxy, bright slow rotators (Capaccioli et al. 1992; Kormendy & Bender 1996; Emsellem et al. 2007). The velocity dispersion profiles are shaped by the combination of orbit structure and mass distribution, but it is still unclear which of these drives the halo differences between the two galaxy classes.

In inferring the mass and the orbital structure, the dynamical modelling of the PN data has been so far focused on intermediate luminosity systems with declining dispersion profiles (R+03; D+07; De Lorenzi et al. 2008, hereafter DL+08; De Lorenzi et al. 2009, hereafter DL+09; N+09; Rodionov & Athanassoula 2010; cf. Weijmans et al. 2009; Forestell & Gebhardt 2010). N+09 summarized the results, comparing constraints from PNe with the ones on group central “bright” galaxies from X-rays and globular clusters, and drew the tentative conclusion that there is a strong transition between low- and high-concentration DM haloes. Such a peculiar trend could imply a transition in the role of baryons in shaping DM haloes, or a problem with the

Table 1. NGC 4374: basic data for the dynamical analysis.

Parameter	Value	Reference
R.A. (J2000)	12 ^h 25 ^m 03.7 ^s	NED ¹
Decl. (J2000)	+12° 53′ 13″	NED
v_{sys}	1060 km s ⁻¹	NED
$(m - M)_0$	31.17 mag	Tonry et al. (2001) ²
A_V	0.131 mag	Schlegel et al. (1998)
M_V	-22.41 ± 0.10 mag	Sec. 2.1
R_e from SB fit	113.5″ ± 11	Sec. 2.1
R_e adopted	72.5″ ± 6	Sec. 2.1
σ_0	284 km s ⁻¹	HyperLeda ³

NOTES – (1): <http://nedwww.ipac.caltech.edu/>
(2): corrected by -0.16 mag (see Jensen et al. 2003)
(3): <http://leda.univ-lyon1.fr/> (Paturel et al. 2003)
(4): adopting our $(m - M)_0$.

Λ CDM paradigm itself (see also N+05, and N+09 for a detailed discussion).

The picture is far from clear and calls for more extensive analysis. In this paper we investigate the giant galaxy NGC 4374 (M84) using the stellar and PN kinematics data previously presented in C+09. This is a bright E1 galaxy ($\sim 3L^*$ luminosity) located in the Virgo cluster core region. It may be part of a group falling into the Virgo cluster, but it does not show any signs of being a group-central object. Mass models have been constructed by Kronawitter et al. (2000, hereafter K+00), and Cappellari et al. (2006, hereafter C+06) using stellar kinematics within 1 R_e (the effective radius enclosing half the projected light). Extensive ground-based photometry has been analyzed in Kormendy et al. (2009).

NGC 4374 hosts an AGN as demonstrated by X-ray jet emission (Finoguenov & Jones 2001) correlated with two radio lobes (Laing & Bridle 1987), and connected to a massive central black hole (Bower et al. 1998). The hot interstellar gas in the galaxy is highly disturbed and not amenable to a standard X-ray based mass analysis (Finoguenov et al. 2008).

As a representative of the “bright-ETG” population with a flat-dispersion profile (see e.g. C+09), NGC 4374 provides an important opportunity to investigate the difference between the low-concentrations inferred from PNe and the high-concentrations from globular clusters and X-rays. These tracers have so far been applied to different classes of galaxies, which suggests the possibility that there are systematic differences in the mass tracers themselves. Alternatively, the mass inferences may turn out to be robust to the type of tracer used, and then should be examined in more detail to see if they are explainable within the Λ CDM framework.

The paper is organized as follows. Section 2 presents the NGC 4374 PN system properties like radial density, velocity dispersion and kurtosis profile, comparing them with the stellar light surface brightness and kinematical profiles. We analyze the system’s dynamics in Section 3 and discuss the results in relation to previous galaxy analyses in Section 4. In Section 5 we draw conclusions. An Appendix covers model variations with an alternative choice of rejected outlier PNe.

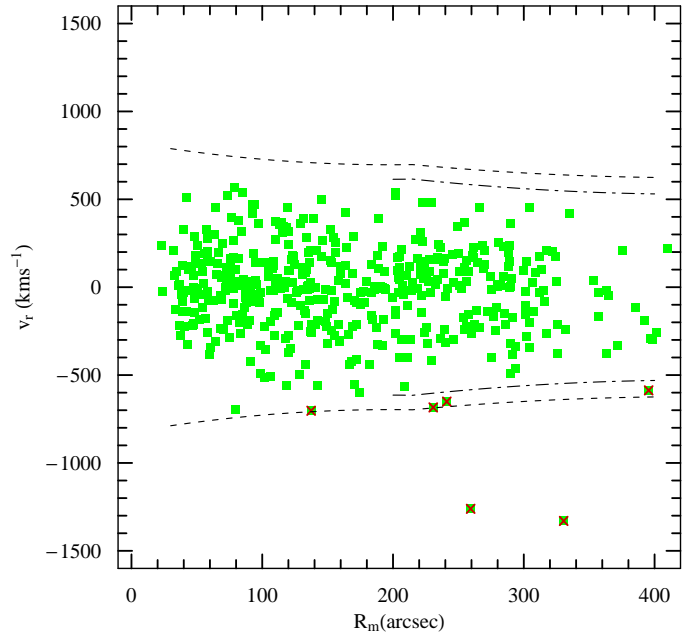


Figure 1. Distribution of line-of-sight velocities of PN candidates around NGC 4374, as a function of radius, and relative to the systemic velocity (1060 km s⁻¹). Red \times symbols mark objects designated as outliers and green boxes show the *bona fide* PNe. The dotted line shows the 3 σ velocity envelope. The dash-dotted line the 3 σ velocity envelope corrected by the energy injected by the interaction with NGC 4406 (see Appendix).

2 PN SYSTEM PROPERTIES

The data that will be the basis of our dynamical modelling were presented in C+09, which can be consulted for details of observations and data reduction. Deep long-slit stellar spectra were obtained with the VLT+FOR2 spectrograph along the major and minor axes, and 454 PN candidate velocities with the WHT+PN.S. Observations were carried out on two different runs (1–4 Apr 2005, 29–3 Mar 2006) with quite uniform seeing conditions ($\sim 1.2''$). To accommodate the anticipated kinematics range for the galaxy, filter AB at 0° tilt was used, which has an estimated bandpass of $\sim 5026\text{\AA}$ with 36 \AA FWHM.

Here we begin by revisiting some of the data characterization steps with a few differences optimized for the dynamical analysis.

We present the basic properties of the field stars and PNe in NGC 4374, including their distributions in space and velocity. Since an important assumption of our models is that the PNe are a fair tracer population of the field stars, we compare throughout the properties of the stars and PNe. The full line-of-sight velocity field of the PN system of the galaxy has been discussed in C+09 (see, e.g., their Fig. 3). Both the galaxy light and the PN distribution appear round so we will assume spherical symmetry and use, as radial distance from the galaxy centre, the projected intermediate axis R_m , which is related to the semi-major axis radius R_a and ellipticity ϵ by $R_m \equiv R_a(1 - \epsilon)^{1/2}$ [where $\epsilon(R_a)$ is taken from Kormendy et al. 2009].

For the dynamical analysis in this paper, we have con-

centrated on identifying possible outliers which could be due to unresolved background emission-line galaxies, or to PN pair mismatches in crowded regions or in the case of NGC 4374, to PNe belonging to the nearby giant elliptical NGC 4406. As done in D+07 and N+09, we have combined a 3σ clipping criterion plus a “friendless” algorithm introduced in Merrett et al. (2003). In Fig. 1 we show the PN individual velocities versus R_m where we have marked with red crosses the PNe which were either outside the 3σ velocity envelope or turned out to be friendless (i.e. having a velocity more than 3σ away from the average velocity of their 20 nearest neighbours).

Using this approach we exclude 6 out of 457 PNe from the C+09 catalog. Some of these 6 differ from the outliers identified by C+09 because the friendless algorithm is now applied to the raw data set rather than a point-symmetrized version. The outliers show a notable asymmetry with respect to the systemic velocity, which motivates the use of the non-symmetrized friendless algorithm, and which is probably due to a fly-by encounter of a nearby giant galaxy as discussed in the Appendix.

The outlier selection is not foolproof and is a potential source of bias in the analysis.

In the Appendix, we also explore the impact on the dynamical models of varying the outlier selection, and find that the mass results are not significantly affected by changes in the outlier selection, while the anisotropy inferences are sensitive to the classification of a small number of objects. Follow-up spectroscopy of these objects would clearly be valuable.

We next examine the spatial distribution of the final catalog in §2.1, and the velocity dispersion and the kurtosis in §2.2.

2.1 Surface photometry and PN spatial distribution

For the galaxy light, we have used the surface photometry from Kormendy et al. (2009) as in C+09, but we have reduced the major/minor axis to a single profile as a function of R_m , as shown in Fig. 2 [hereafter, R_m and R will be used interchangeably for the intermediate-axis radius].

To characterize the stellar luminosity profile, we parametrize the surface brightness (SB) profile by the Sérsic law:

$$\mu(R) - \mu(0) \propto (R/a_S)^{1/m}, \quad (1)$$

where a_S is a scale length and m describes the “curvature” of the profile (Sérsic 1968). Fitting the dataset from $R = 1''$ to $465''$, we find $a_S = 0.00003''$, $m = 6.11$, and $\mu_0 = 9.74 \text{ mag arcsec}^{-2}$, and $R_e = 113.5''$. Other values obtained in the literature include $51''$ from de Vaucouleurs et al. (1991), $53''$ from Blakeslee et al. (2001), $72.5''$ from C+06, $93''$ from Hopkins et al. (2009), $114''$ and $142''$ from (Kormendy et al. 2009; along the semi-major axis), and $204''$ from Janowiecki et al. (2010).

These differences do not mean that the galaxy’s luminosity profile is not reasonably well known over the region which we will be modelling, but that for high-Sérsic-index galaxies, certain characteristic quantities such as R_e and total luminosity require considerable extrapolation and are poorly constrained.

This is not a problem that we will solve overnight, and for the sake of using an R_e parameter that is equivalent to the most common usage in observations and theory, we adopt $R_e = 72.5''$ from the wide-field $R^{1/4}$ growth-curve fitting of C+06. This differs from our approach in C+09, where for the sake of uniformity we adopted the Blakeslee et al. (2001) values, which will not be reliable for very extended galaxies because of the narrow imaging fields used. Our modelling will all be conducted in physical units, so this choice of R_e impacts only the quoting of radial ranges in some cases, and the comparisons to simulated galaxies.

With our full Sérsic solution, the extinction-corrected total luminosity in the V -band is $7.64 \times 10^{10} L_{V,\odot}$, or $M_V = -22.4$; the uncertainties in the outer surface brightness profile yield a (model-dependent) total luminosity uncertainty of $\sim 10\text{--}15\%$. These and other global parameters for NGC 4374 are listed in Table 1. For practical use in the Jeans modeling, we have also produced a smoothed density profile from the data made by a combination of a simple interpolation of the data up to $290''$ and our Sérsic model outside this radius.

We next compare the spatial density of the PNe with the field stars, using the PN number density complete to $m^* + 1.1$ (see C+09, Table 7). Note that while C+09 used R_a , we bin the data using R_m .

Given an arbitrary normalization, the *PN profile matches the stellar photometry remarkably well* (Fig. 2)—as also generally found in a larger sample of galaxies by C+09.

2.2 The dispersion and kurtosis profiles

The rotation and velocity dispersion along the major and minor axes of NGC 4374 have been discussed in C+09 (their fig. 7), together with the 2D radial velocity field (their fig. 3). For the spherical analysis in this paper, we reduce these data to a single average velocity dispersion profile after having rescaled the two axes to the intermediate-axis radius R_m .

To obtain the azimuthally averaged profile, the rotation and true dispersion profile are folded into an root-mean-square velocity profile $v_{\text{RMS}} = \sqrt{v^2 + \sigma^2}$ ¹, where v and σ are the rotation and dispersion components respectively². This RMS velocity is a measure of the total kinetic energy, and we henceforth loosely refer to it as the velocity dispersion or VD. We combine the stellar data from the different axes by averaging, while folding the (small) systematic

¹ In the following we will use spherical Jeans equations for non-rotating systems. Although NGC 4374 has no significant rotation, the use of the v_{RMS} will ensure that there is no rotation contribution missing in the equilibrium balance.

² In the long-slit stellar data, v and σ are not the true classical moments but fit parameters in a Gauss-Hermite series which includes the higher-order moments h_3 and h_4 . In principle, we should convert these fit parameters into revised estimates of the classical moments, e.g. using equation 18 of van der Marel & Franx (1993). Doing so would lower the outer stellar dispersion profiles by $\sim 10\%$. However, it is notoriously difficult to extract reliable measurements of higher-order moments (e.g. Shapiro et al. 2006), and we are not confident that the h_4 measurements in this case are accurate. To avoid introducing spurious corrections to the kinematics, we therefore assume the v and σ fit parameters are good estimates of the classical moments.

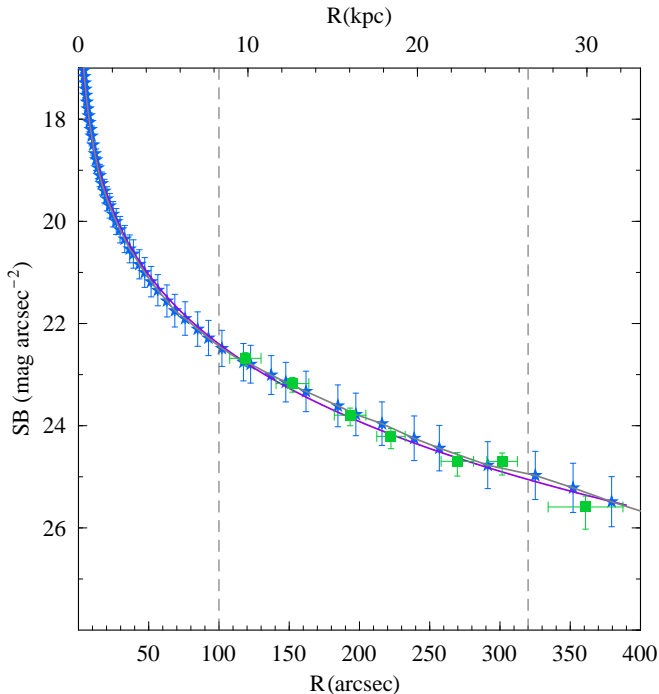


Figure 2. Radial surface density profiles of the field stars (V -band; blue star symbols) and of the PNe (green squares) in NGC 4374. The PN number counts have been corrected for spatial incompleteness, and arbitrarily normalized to match the stellar data. The vertical error bars of the PN data in this and in the following figures represent the 1σ uncertainties (based in this case on counting statistics and completeness correction uncertainties), while the horizontal error bars show 68% of the radial range of the PNe in each bin. The purple curve is a Sérsic model fit to the stellar photometry, and the gray solid curve is the interpolating profile. The vertical dashed lines show the spatial completeness interval of the PN system.

differences into the final uncertainties³. The PN VD is calculated using a classical expression for the variance of the discrete velocities around the systemic velocity. Note that the rotation amplitude of $\sim 50 \text{ km s}^{-1}$ is not dynamically significant compared to the dispersion of $\sim 200\text{--}250 \text{ km s}^{-1}$.

The resulting “dispersion” data are plotted in Fig. 3. Overall, the use of the full PN sample in the azimuthal averaged profile allows us to map the kinematics of the galaxy out to $\sim 340''$ which is 20% farther out than the major/minor axis analysis performed in C+09.

The dispersion decreases sharply from the centre out to $50''$ where the VD from the long slit data flattens at $\sim 220 \text{ km s}^{-1}$. *The PN data are consistent with the stellar absorption estimates in the region of overlap* and possibly show a rise of the VD profile from $100''$ with a peak of $\sim 240 \text{ km s}^{-1}$ at $170''$ (corresponding to about 15 kpc for our

³ The uncertainties in the PN dispersion use a classical analytic formula that assumes a Gaussian distribution, i.e. $\Delta v_{\text{RMS}} \sim \sqrt{\Sigma_i v_i^2 / 2N^2}$. We expect this approximation to produce accurate results in realistic systems (Napolitano et al. 2001), and we have carried out additional Monte Carlo simulations of a simplified galaxy with radial orbits, finding that the dispersion is very accurately recovered with our estimator, with a possible bias to be $\sim 5\%$ too high.

adopted distance) and a subsequent decrease to the original value of 220 km s^{-1} where the VD stays flat out to the last data point ($\sim 340''$ or 27 kpc, i.e. $\sim 5 R_e$). This makes NGC 4374 a prototypical system with a flat dispersion profile, although the uncertainty on the R_e estimate (e.g. for $R_e = 204''$ the last data point is at $\sim 1.8 R_e$) provides a warning that we may not be sampling far enough from the center to probe the full dynamical range of the system. More extended data (ideally in the direction opposite to the nearby galaxy NGC 4406 where it is more likely that the stellar kinematics is undisturbed) would clarify whether the velocity dispersion remains flat farther out, starts to decrease as observed in the intermediate luminosity sample or begins to rise as the cluster potential is probed.

The v_{RMS} shows a bump at around $15''$ which is also seen in the major and minor profiles and might be related to some kinematical substructure⁴ which is not evident in the photometric profile (see Fig. 2). As we are mainly interested in modelling the galaxy outskirts, the presence of these wiggles in the kinematical profile will not affect our analysis.

The nearly flat dispersion profile in Fig. 3 corresponds to an asymptotic slope of -0.07 ± 0.07 which is in clear contrast with the decreasing profiles found in intermediate luminosity galaxies, with typical power-law exponents of -0.2 to -0.6 (see R+03; D+07; N+09). Napolitano et al. 2008 and C+09 identified a possible dichotomy of early-type galaxies based on these dispersion slope differences, and we will here investigate further the dynamical implications for NGC 4374.

We next consider higher-order velocity information. We quantify the shapes of the stellar and PN line-of-sight velocity distributions (LOSVDs) in NGC 4374 using a classical dimensionless kurtosis, $\kappa \equiv \overline{v^4} / (\overline{v^2})^2 - 3$ (see Joanes & Gill 1998 for exact expressions and uncertainties⁵). Broadly speaking, we can expect that $\kappa \simeq 0$ is a fair indication of isotropic orbits, $\kappa < 0$ is pertinent to tangential orbits and $\kappa > 0$ for radial orbits.

In Fig. 3 we have combined the PN estimates with the stellar equivalent by converting the long slit stellar Gauss-Hermite coefficient h_4 (van der Marel & Franx 1993; Gerhard 1993) into kurtosis estimates using the approximate relation $\kappa \simeq 8\sqrt{6}h_4$.

The PN kurtosis is consistent with the stellar properties in the region of overlap. Thanks to the large statistical sample, the PN data points show error bars which are fairly similar to stellar estimates, based on the best quality stellar absorption line data. The total kurtosis profile is consistent with zero at all radii and has a median (calculated over all datapoints) of 0.05 ± 0.19 .

Our previous analyses of NGC 3379 and NGC 4494 indicated global $\kappa \sim +0.2$ and $+0.6$, respectively. However, most of this difference is driven by the data inside R_e , where previous work with larger galaxy samples has indicated that any correlations between the fourth moment and other galaxy

⁴ This may be related to the central dust ring clearly seen in optical imaging of the galaxy (Jaffe et al. 1994).

⁵ Monte Carlo simulations based on Napolitano et al. (2001) models have demonstrated accurate recovery of the kurtosis using our estimator, with a systematic deviation of no more than ~ 0.1 , see also N+09.

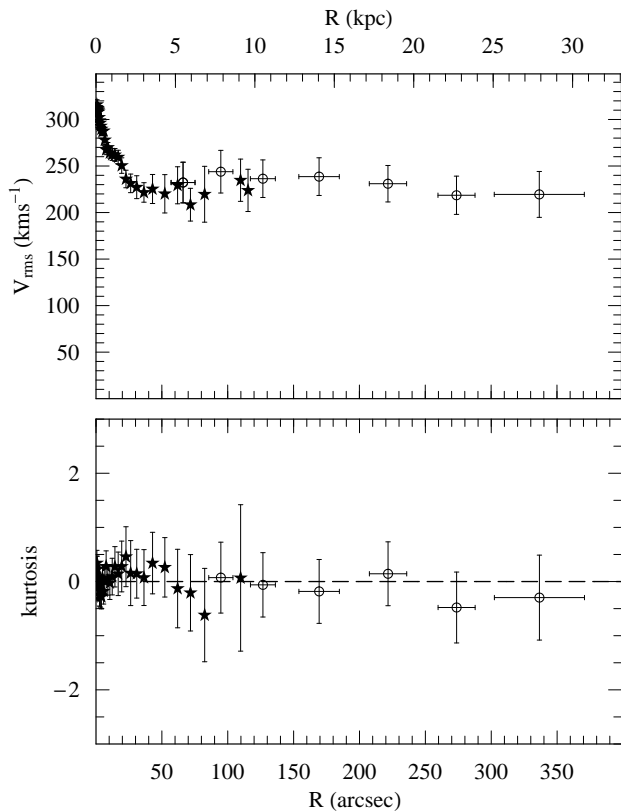


Figure 3. Composite projected RMS velocity and kurtosis profiles of NGC 4374, with data from stars (filled star symbols) and PNe (open circles). Separated profiles of rotation and true dispersion can be seen in C+09.

properties are subtle (Bender et al. 1994; Krajnović et al. 2008).

In the outer parts, all three galaxies are similarly consistent with zero kurtosis, and it will be interesting to see if any patterns emerge with a large sample. However, as we will see in the next Section, interpreting the orbital anisotropy implications of the kurtosis requires detailed modelling.

3 DYNAMICAL MODELS

We present a suite of Jeans dynamical models following the same scheme as in N+09, to which we refer the reader for more details of the analysis. We will combine the photometric and kinematical data for the stars and PNe in NGC 4374 into integrated models in order to derive the mass profile and the orbital distribution of the galaxy and finally test whether or not it hosts a massive dark halo compatible with the Λ CDM predictions.

Although there are other dynamical procedures such as Schwarzschild’s method and made-to-measure particle methods (e.g. R+03; Chanamé et al. 2008; DL+08) that have been applied to discrete velocity data and are more robust than our Jeans approach, the latter is computationally faster and somewhat more intuitive. Furthermore it allows a much larger flexibility on the range of galaxy potentials to be used. In the following we briefly remind the main steps of our dynamical procedures.

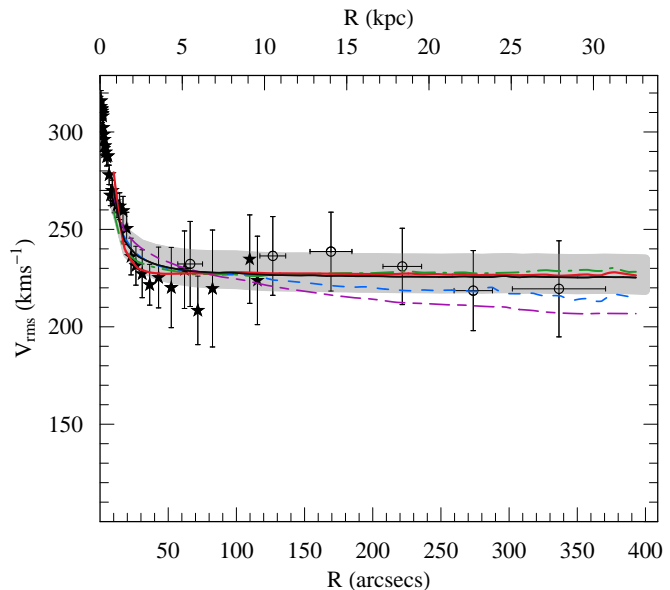


Figure 4. Composite projected velocity dispersion profile of NGC 4374, with data from stars (filled star symbols) and PNe (open circles). The black solid curve shows the pseudo-inversion mass model to fit the PN data outside $10''$ for the isotropic case, with the shaded regions showing the 1σ significance of the fit. The short dashed blue curve shows the solution for $\beta = 0.5$, the dot-dashed green curve the one for $\beta = -0.5$. The long-short-dashed violet line shows the solution for the cosmological motivated $\beta(r)$ profile as in Eq. 5. The thick red solid line shows the heuristic $\beta(r)$ model adopted in Sect. 3.5.

In the different formulations of the Jeans equations we will assume spherical symmetry. This is a reasonable approximation because the round and boxy stellar isophotes of NGC 4374 (average ellipticity $\langle \epsilon \rangle = 0.13$ and $\langle a_4 \rangle = -0.4$; see C+09), and the small $V/\sigma = 0.03$ (Cappellari et al. 2007)⁶ make the system a typical boxy–slow rotator which is highly unlikely to be very flattened intrinsically.

Another basic assumption of our analysis is that stars and PNe are all drawn from the same underlying dynamical tracer population, which is well motivated by the agreement between the stellar and PN properties (§2.1 and 2.2). We will also in general omit the stellar kinematics data inside $10''$ from our model fits, since there appears to be a strong dynamical change in the nuclear region which our smooth Jeans models are not designed to reproduce (partially produced by a massive black hole; Bower et al. 1998⁷).

We begin with a simple non-parametric model in §3.1, then introduce multi-component mass-models in §3.2 and additional dynamical methods in §3.3. The multi-component results are presented in §3.4–3.6 and the mass profiles summarized in §3.7.

⁶ Their fig. 3 illustrates an estimated family of deprojections for this galaxy, with the most flattened solution having $\epsilon \sim 0.2$.

⁷ Here Bower et al. (1998) estimate a black hole mass of $M_{\text{BH}} \sim 1.5 \times 10^9 M_{\odot}$ which implies a sphere of influence of radius $r_h \sim 1.7''$, where we have defined r_h as the radius where $M_*(r < r_h) = 2M_{\text{BH}}$, with $M_*(r)$ corresponding to the Kroupa IMF.

3.1 Pseudo-inversion mass model

We start with a phenomenological approach introduced in R+03 and followed in D+07 and N+09, used to convert the observed kinematics into a mass profile $M(r)$. This approach has the advantage that it is computationally light, does not involve Abel inversion integrals, and does not assume any form for $M(r)$, nor a stellar M/L value (which will be discussed later in this Section). A disadvantage is that it does not allow a direct test of any theoretical prediction (which we will do in the next Sections).

For the benefit of readers not familiar with this procedure, we summarize in the following its basic steps:

(i) Adopt a simple smooth parametric function for the intrinsic radial velocity dispersion profile:

$$\sigma_r(r) = \sigma_0 \left[1 + \left(\frac{r}{r+r_0} \right)^\eta \right]^{-1}, \quad (2)$$

where σ_0, r_0, η are a minimalistic set of free parameters. This model is adopted to reproduce the flat dispersion profile in the outer galaxy regions and is different from those adopted in D+07 and N+09 which were constructed to match steeply decreasing velocity dispersion profiles.

(ii) Assume a given anisotropy profile, often constant or parametrized as a simple function:

$$\beta(r) \equiv 1 - \sigma_\theta^2 / \sigma_r^2, \quad (3)$$

where σ_θ and σ_r are the spherically-symmetric tangential and radial components of the velocity dispersion ellipsoid, expressed in spherical coordinates⁸.

(iii) Project the line-of-sight components of the 3-D velocity dispersions σ_r and σ_θ for comparison with the line-of-sight velocity dispersion data $\sigma_{\text{los}}(R)$.

(iv) Iteratively adjust the free parameters in Eq. 2, to best fit the model to the observed dispersion profile.

(v) Use the best-fit model (Eq. 2) in the Jeans equation 4-55 of Binney & Tremaine (1987) to calculate $M(r)$:

$$M(r) = -\frac{\sigma_r^2 r}{G} \left(\frac{d \ln j_*}{d \ln r} + \frac{d \ln \sigma_r^2}{d \ln r} + 2\beta \right), \quad (4)$$

where $j_*(r)$ is the spatial density of the PNe, and corresponds to an Abel deprojection of a smoothed density law as in §2.1. Additional quantities may then be computed, such as the cumulative M/L .

Starting with the isotropic case ($\beta = 0$), we find that the simple model (2) is able to fit the dispersion data well (Fig. 4), with some systematic discrepancies at $\sim 40''$ that we will improve upon with more complicated models below. The resulting M/L profile increases steeply with the radius (Fig. 5), providing a strong indication for the presence of an extended DM halo. Note that the shaded regions in Figs. 4 and 5 along with the various uncertainties quoted below account for the 1- σ statistical confidence region in the parameter space (σ_0, r_0, η) of the dynamical model.

The central dynamical $(M/L)_V = 6.5$ can also be compared with independent stellar population analyses of the stellar M/L , Υ_* . Assuming a Kroupa (2001) IMF, Tortora et al. (2009) found $\Upsilon_* \sim 3-4.5 \Upsilon_{\odot,V}$, while

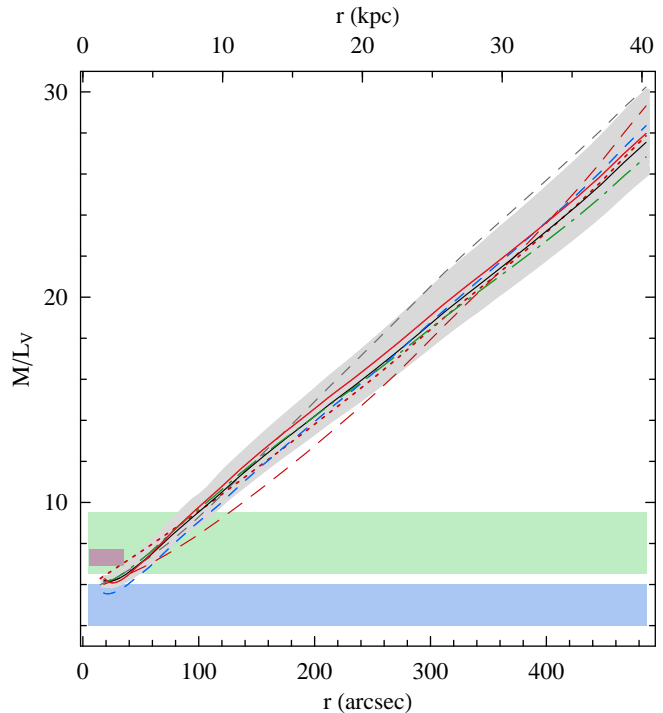


Figure 5. Cumulative V-band mass-to-light ratio (M/L) of NGC 4374 (note that the vertical axis starts from $\Upsilon_{\odot,V} = 3$). The curves based on the pseudo-mass inversion method are colour coded as in Fig. 4. We also add some of the models from the Jeans analysis in §3.3: the dotted red curve is the “NFW + $\beta(r)$ ”, the dashed red curve is the same model with adiabatic contraction [“NFW + AC + $\beta(r)$ ”], and the dashed gray line is the logarithmic potential model with $\beta(r)$ (see §3.5 and §3.6). The horizontal blue shaded region shows the stellar M/L and its uncertainty for the Kroupa IMF, while the green one is for the Salpeter IMF. The small purple shaded region is the dynamical M/L estimate from C+06. See text for details.

Gerhard et al. (2001) found $\Upsilon_* \sim 4.5-6.0 \Upsilon_{\odot,V}$ (where we have in both cases converted from B - to V -band). C+06 found $\Upsilon_* = 3.08 \Upsilon_{\odot}$ in I -band which we convert to $\Upsilon_* \simeq 5.14 \Upsilon_{\odot,V}$ after detailed comparison of the SB profiles. (Note that their Schwarzschild modelling analysis implies a dynamical $\Upsilon \simeq 7.3 \pm 0.4 \Upsilon_{\odot,V}$ in the central regions, which agrees with our Jeans results, as shown in Fig. 5.)

We can reasonably assume $\Upsilon_* \sim 4-6 \Upsilon_{\odot,V}$ for a Kroupa IMF, which corresponds to $\sim 6.5-9.5 \Upsilon_{\odot,V}$ for a Salpeter (1955) IMF (see Fig. 4). Therefore the dynamical M/L is suggestive of some dark matter inside R_e ($72.5''$) for the case of Kroupa but not Salpeter. In the following we will consider the stellar M/L based on the Kroupa IMF as the reference results, since there are arguments to consider this one as a universal IMF (Kroupa 2001).

Our last datapoint ($\sim 340''$) is close to $\sim 5 R_e$, which is a benchmark distance for the mass profiles (see R+03, D+07 and N+09): here we find that the V -band M/L within this radius is $\Upsilon_{5,V} \sim 20 \pm 2 \Upsilon_{\odot,V}$ ⁹. The anisotropy is accounted for in step (ii) of the procedure by adopting constant values

⁸ Due to the modest rotation of the galaxy, we expect the spherical approximation not to cause any significant systematic issues.

⁹ Hereafter we are deliberately neglecting the uncertainty on R_e which we have seen are unreasonably large and scale all the results for our assumed R_e .

of $\beta = \pm 0.5$ as a plausible (though not exhaustive) range of the stellar anisotropy. The fits to the data are just as good as for the isotropic case as shown in Fig. 4.

In Fig. 5 we show the $M/L(r)$ profiles corresponding to the three β values. Assuming $\beta = +0.5$ implies a smaller central M/L ($\sim 5.5 \Upsilon_{\odot,V}$) but a steeper M/L profile than the case of $\beta = 0$, while $\beta = -0.5$ implies a larger central M/L ($\sim 7\Upsilon_{\odot,V}$) and a shallower M/L profile outside $1 R_e$ (with the M/L consistent with the isotropic profile at all radii in either cases). In all cases a constant M/L is excluded at more than 3σ and DM starts dominating already at $1 R_e$, assuming a Kroupa IMF, and at $\sim 2 R_e$ for the Salpeter IMF case.

Our outer M/L results are relatively insensitive to the anisotropy assumed because of a geometrical effect in certain regimes in radius that causes anisotropy differences to cancel out when projected to line-of-sight velocity dispersions (cf. Gerhard 1993, Fig. 8; van der Marel 1994, Figs. 10 and 11; Wolf et al. 2010). This ‘‘pinch point’’ occurs where the 3D log slopes of the tracer density profile α and the velocity dispersion γ add up to $(\alpha + \gamma) \simeq -3$ (see Dekel et al. 2005 Eq. 2). In a bright elliptical galaxy like N4374, the high Sersic index n , the large scale-length, and the flat dispersion profile combine to push the pinch point to fairly large radii: $\sim 100''$ in this case. This robustness of the mass inference contrasts with the case of galaxies with steeply declining dispersion profiles, where the mass-anisotropy degeneracy is particularly severe (DL+08; DL+09).

We have also tested the anisotropy profile based on theoretical expectations from merging collisionless systems as derived from ML05:

$$\beta(r) = \beta_0 \frac{r}{r + r_a}, \quad (5)$$

where $\beta_0 \simeq 0.5$ and $r_a \simeq 1.4 R_e$ (based on the merger simulations of D+05). Adopting this profile with $r_a = 101''$, we find that the VD profile matches slightly better the central regions, but it fits poorly the large radii datapoints. In this respect Eq. 5 seems to be ineffective in reproducing the intrinsic anisotropy of the galaxy (given the limits of the simple parametrization assumed in equation 2)¹⁰ However, the fact that radial anisotropy produces a better fit to the central VD while $\beta = 0$ matches the outer parts of the galaxy suggests that a more complicated $\beta(r)$ profile than the one in Eq. 5 should be applied to NGC 4374.

For instance, looking at the kurtosis profile in Fig. 3, one suspects that a $\beta(r)$ profile which is isotropic in the very central regions ($R < 5''$) and in the outer parts ($R \gtrsim 70''$) and radially anisotropic in between ($R \sim 5'' - 70''$) might do a better job. Following this heuristic approach we adopt the following formula:

$$\beta(\xi) = \beta_0 \frac{\xi^{1/2}}{\xi^2 + 1}, \quad (6)$$

where $\beta_0 = 0.6$ and $\xi = r/r_a$ with $r_a \sim 30''$ (see also Section 3.5). This $\beta(r)$ profile is significantly different from the simulation-based Eq. 5 but similar to the $\beta(r)$ found from the detailed dynamical models of K+00 for NGC 4374 (see

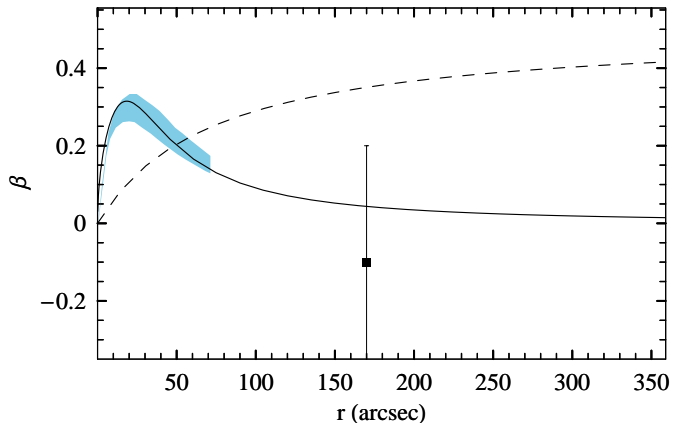


Figure 6. The heuristic $\beta(r)$ profile in Eq. 6 (solid line) is compared with the simulation based $\beta(r)$ (dashed line) from ML05 as in Eq. 5 and the modelled $\beta(r)$ from Kronawitter et al. 2000 (shaded region). Here only the radial range covered by the Kronawitter et al. model is shown: the matching with the heuristic $\beta(r)$ is good, while the ML05 formula predicts radial anisotropy at much larger distances from the centre. The anisotropy value derived from direct kurtosis inferences (see §3.3) is also shown with 1σ error bars.

Fig. 6) as well as for some other galaxies in their sample (e.g. NGC 4278, NGC 4472, NGC 4486, NGC 5846). In this case the best fit to the VD is improved as shown in Fig. 4 (red curve; we will come back to this issue in §3.5). The corresponding M/L profile has a central value which is closer to the isotropic solution ($\sim 6.5\Upsilon_{\odot,V}$) and becomes slightly larger outward, finally converging to the isotropic case asymptotically.

The overall plausible range for the benchmark-radius M/L of NGC 4374 is $\Upsilon_{5,V} = 18\text{--}24 \Upsilon_{\odot,V}$ (including both statistical uncertainties as well as the systematic anisotropy uncertainties, given the range of $\beta(r)$ profiles that we allow). This result is significantly larger than the typical M/L found for the intermediate-luminosity galaxy sample studied so far with the PN.S (see e.g. R+03, D+07, DL+09 and N+09), but more similar to the M/L estimates found in bright systems using globular clusters and X-rays (e.g. Humphrey et al. 2006; Romanowsky et al. 2009; Schuberth et al. 2010; Das et al. 2010).

The steep increase of the M/L with radius can be quantified through the dimensionless M/L gradient (introduced by N+05):

$$\nabla_{\ell} \Upsilon \equiv \frac{R_e \Delta \Upsilon}{\Upsilon_{\text{in}} \Delta R}, \quad (7)$$

where Υ_{in} is the central dynamical M/L . For NGC 4374 we find $\nabla_{\ell} \Upsilon = 0.5\text{--}0.7$, which places this galaxy among the systems with larger $\nabla_{\ell} \Upsilon$ which are discussed in N+05 as very dark-matter dominated. As a comparison, for NGC 3379 and NGC 4494 we found $\nabla_{\ell} \Upsilon$ in the range -0.05 to 0.25 .

3.2 Multi-component models: mass profiles

The second strategy for our dynamical analysis again uses a Jeans analysis but begins with parameterized mass profiles and projects the predicted kinematics for comparison to the data. Following N+09, the inclusion of higher veloc-

¹⁰ We tried out a wider range of r_a : for smaller r_a the predicted dispersion was still lower than the data, and for larger r_a the dispersion progressively approached the isotropic case.

ity moments (kurtosis) in the Jeans analysis is expected to alleviate the mass-anisotropy degeneracy.

In our equations, we will adopt two-component mass models consisting of a luminous field star distribution plus a DM halo. The total gravitational potential may thus be expressed as $\Phi = \Phi_* + \Phi_d$. The stellar gravitational potential $\Phi_*(r)$ is derived from the stellar luminosity $j_*(r)$ ¹¹, combined with some assumed constant Υ_* .

Our mass models as described below use for the DM either an NFW profile (§3.2.1) or a pseudo-isothermal form (§3.2.2).

3.2.1 NFW model

Our reference mass models aims at testing the predictions from simulations of collisionless DM halo formation in a Λ CDM cosmology. In this case the DM density takes the approximate form of an NFW profile:

$$\rho_d(r) = \frac{\rho_s}{(r/r_s)(1+r/r_s)^2}, \quad (8)$$

where ρ_s and r_s are the characteristic density and scale radius of the halo. The cumulative dark halo mass is

$$M_d(r) = 4\pi\rho_s r_s^3 A(r/r_s), \quad (9)$$

where

$$A(x) \equiv \ln(1+x) - \frac{x}{1+x}. \quad (10)$$

The potential is:

$$\Phi_d(r) = \frac{4\pi G \rho_s r_s^3}{r} \ln\left(\frac{r_s}{r+r_s}\right), \quad (11)$$

where G is the gravitational constant.

The three free parameters describing the NFW mass model are thus Υ_* , ρ_s and r_s . The halo can alternatively be parametrized by the virial mass and concentration, $M_{\text{vir}} \equiv 4\pi\Delta_{\text{vir}}\rho_{\text{crit}}r_{\text{vir}}^3/3$ and $c_{\text{vir}} \equiv r_{\text{vir}}/r_s$, where the critical density is $\rho_{\text{crit}} = 1.37 \times 10^{-7} M_\odot \text{pc}^{-3}$ and the virial overdensity value is $\Delta_{\text{vir}} \simeq 100$.

The expected values for these model parameters are not arbitrary in Λ CDM. For instance, in a collisionless Λ CDM universe with WMAP5 parameters, the following mean relation is expected between mass and concentration¹²:

$$c_{\text{vir}}(M_{\text{vir}}) \simeq 12 \left(\frac{M_{\text{vir}}}{10^{11} M_\odot} \right)^{-0.094} \quad (12)$$

which has a 1 σ scatter of 0.11 dex, and is valid for $z = 0$, $\Omega_m = 0.3$, $\Omega_\Lambda = 0.7$, $h = 0.7$, and $\sigma_8 = 0.8$ (Macciò et al. 2008). For comparing with models parameterized by the scale radius r_s and density ρ_s (e.g. Eq. 8), we find that Eq. 12 is equivalent to the following relation:

¹¹ This is obtained by Abell inversion of the observed SB in the central regions and the extrapolation to infinity according to the Sérsic model of §2.1.

¹² For sake of completeness we also report here the WMAP1 equations (see N+09 for details):

$$c_{\text{vir}}(M_{\text{vir}}) \simeq 18 \left(\frac{M_{\text{vir}}}{h^{-1} 10^{11} M_\odot} \right)^{-0.125}$$

and

$$\rho_s \simeq \left(\frac{r_s}{10 \text{pc}} \right)^{-2/3} M_\odot \text{pc}^{-3}.$$

$$\rho_s \simeq 0.29 \left(\frac{r_s}{10 \text{pc}} \right)^{-0.53} M_\odot \text{pc}^{-3}. \quad (13)$$

where the scatter in ρ_s at fixed r_s is a factor of 1.3. Note that in N+09 we used Λ CDM halo predictions based on WMAP1 parameters, which implied $\sim 30\%$ higher concentrations than WMAP5.

3.2.2 LOG model

Our alternative mass model consists of a logarithmic potential (Binney & Tremaine 1987 §2.2.2) which was motivated by observations of spiral galaxy rotation curves (see e.g. Persic et al. 1996). The potential is:

$$\Phi_d(r) = \frac{v_0^2}{2} \ln(r_0^2 + r^2), \quad (14)$$

where v_0 and r_0 are the asymptotic circular velocity and core radius of the halo. The corresponding DM density and cumulative mass profiles are respectively:

$$\rho_d(r) = \frac{v_0^2(3r_0^2 + r^2)}{4\pi G(r_0^2 + r^2)^2}, \quad (15)$$

and

$$M_d(r) = \frac{1}{G} \frac{v_0^2 r^3}{r_0^2 + r^2}. \quad (16)$$

The three free parameters of this “LOG” model are thus Υ_* , v_0 , and r_0 . We define a virial mass relative to the critical density according to the same definition as in §3.2.1 (there is no halo “concentration” in this context).

Unlike the NFW halo with its cuspy r^{-1} density centre, the LOG halo has a constant-density core. At larger radii, the density decreases as r^{-2} , similar to the NFW model near $r = r_s$. This model allows us to maximize the stellar contribution to the central mass, and to test a “minimal DM halo” scenario. Similar models have been successfully used to explain the dynamics of other galaxies of all types (e.g. Fall & Efstathiou 1980; Begeman et al. 1991; K+00; Thomas et al. 2007; Weijmans et al. 2008; DL+08; Pu et al. 2010).

3.3 Multi-component models: dynamical methods

Our Jeans modelling approach has been extensively developed in N+09, to which we refer the reader for the full description of the equations adopted. Basically, in addition to the usual second-order Jeans equations for the velocity dispersion profile, we solve the fourth-order Jeans equations to constrain the LOSVD with kurtosis data and reduce the systematic uncertainties linked to the unknown orbital distribution (e.g. Magorrian & Ballantyne 2001; Lokas 2002; Lokas & Mamon 2003). Although the higher-order Jeans equations are not closed in general, one can adopt a simple choice for the distribution function which makes the problem tractable¹³. This simplification is arbitrary (e.g. β is

¹³ We restrict ourselves here to functions which can be constructed from the energy-dependent distribution function by multiplying it by a function of angular momentum $f(E, L) = f_0(E)L^{-2\beta}$ with $\beta = \text{const}$. This is a widely-used ansatz (Henon 1973; Dejonghe 1986; Wilkinson & Evans 1999; An & Evans

assumed to be constant with radius) and does restrict the generality of our results, but the model is still more general than an assumption of isotropy. In N+09 we demonstrated the utility of this approach for assessing the presence of radial orbits in NGC 4494.

For the sake of clarity, we report in the following the basic steps of our analysis (for more details, see also N+09):

(i) Set up a multi-dimensional grid of model parameter space to explore, including β and the mass profile parameters (Υ_* , ρ_s , r_s) or (Υ_* , v_0 , r_0).

(ii) For each model grid-point, solve the second- and fourth-order Jeans equations.

(iii) Project the internal velocity moments to σ_{los} and κ_{los} .

(iv) Compute the χ^2 statistic, defined as

$$\chi^2 = \sum_{i=1}^{N_{\text{data}}} \left[\frac{p_i^{\text{obs}} - p_i^{\text{mod}}}{\delta p_i^{\text{obs}}} \right]^2, \quad (17)$$

where p_i^{obs} are the observed data points (σ_{los} and κ_{los}), p_i^{mod} the model values, and δp_i^{obs} the uncertainties on the observed values, all at the radial position R_i . We fit the PN data outside $60''$ (where the spatial incompleteness due to the galaxy background is more severe, see also Napolitano et al. 2001) and the stellar data outside $10''$ (see §3).

(v) Find the best fit parameters minimizing the χ^2 . In practice, we find that the VD is affected by both the mass and anisotropy profiles, while the kurtosis is almost entirely driven by the anisotropy.

One interesting side-note is that given the assumptions of our Jeans formalism, we showed in N+09 (Eqs. B10–B12) that if a system has a constant dispersion profile, we can estimate its internal anisotropy β directly from the data without any need for dynamical modelling. This is because the line-of-sight kurtosis κ is then a simple matter of projection effects for a given β and luminosity profile. Therefore at a radius of $\sim 170''$, we estimate that NGC 4374 has an anisotropy of $\beta \simeq -0.1_{-0.4}^{+0.3}$, i.e. it is near-isotropic.

The list of mass models we will explore in the following Sections includes: 1) a no-DM case or self-consistent model where the potential is given by the stellar mass only; 2) a NFW dark halo to be tested against the Λ CDM predictions; 3) a core logarithmic potential. The novelty of this analysis with respect to N+09 and all other dynamical studies on individual ETGs is the inclusion of the effect of the adiabatic contraction of the dark halo, for both the DM halo models as above.

2006), which has the advantage of being easy to integrate even though it does not generalize to the case of $\beta = \beta(r)$ for the fourth-order moment.

3.4 Multi-component model results: no-DM case

In §3.1 we have seen that for NGC 4374, a model with a constant M/L with radius is ruled out by the PN velocity dispersion data. However, the pure-stellar potential ($\rho_s = 0$ or $v_0 = 0$) is the minimal model that can be tried to fit the dispersion and kurtosis data, allowing us to find the maximum stellar content of the galaxy compatible with the inner data points.

The best-fit parameters of the model with an isotropic velocity ellipsoid ($\beta = 0$) are listed in Table 2 together with the χ^2 of the fit.

Given the freedom to adjust Υ_* , the model is able to fit the VD in the central regions ($\lesssim 2R_e$) with a best-fit $\Upsilon_* = 7.5$ (V band). This value is consistent with the SSP estimates based on the Salpeter IMF, and inconsistent with the Kroupa IMF predictions at more than 1σ . We will come back to this issue in the next Section, and note here that, despite the higher Υ_* , the no-DM model fails to reproduce the data since the VD falls off too quickly in the outer regions (Fig. 7, blue dotted line). The gap between the model and the data cannot be removed even by assuming extremely negative β (see e.g. the cyan dot-dashed line for $\beta = -3 \times 10^3$) or by adopting a shallower SB profile as allowed by the fit errors in §2.1.

These Jeans models are not general enough to explore every dynamical solution that is physically possible, but we judge that the data/model differences are large enough to render a constant M/L model highly implausible. We will next proceed with models allowing for the presence of a DM halo to find out what halo parameters are most consistent with the data for the two assumed DM profiles.

3.5 Multi-component model results: NFW model

We next consider the NFW mass model (Section 3.2.1) based on Λ CDM expectations. We initially discuss the case with orbital isotropy in §3.5.1 and show that this matches the data fairly well except near R_e (namely, $20'' - 100''$) where the dispersion (kurtosis) is overestimated (underestimated) by the Jeans models. In §3.5.1 we explore a range of constant and radially-varying β profiles and conclude that a significant radial anisotropy is ruled out at large galactocentric distances, while the $\beta(r)$ profile as in Eq. 6 provides the best match to the data at all radii. Finally we include in our model the effect of adiabatic contraction in §3.5.3 and find that the higher central DM fraction thereby generated allows the data to accommodate a smaller stellar M/L , fully compatible with a Kroupa IMF.

3.5.1 The isotropic model and the stellar M/L issue

We start by assuming isotropy, and find a best fit as shown in Fig. 7 (green dashed), with parameters again reported in Table 2 (“NFW iso”). This solution is a fairly good match to the data, for both the VD and kurtosis profile, which is a further support for the absence of strong anisotropy in the stellar orbital distribution. The best-fit $\Upsilon_* \sim 6.5\Upsilon_{\odot,V}$ is lower than the no-DM case because the central regions contain significant amounts of DM (see §6), although it is still the stellar mass that determines the main kinematical features inside $\sim 100'' \sim 1.2R_e$. This stellar M/L value is

Table 2. Summary of best-fit multi-component model parameters.

Model	β_5^1	Υ_*^2 ($\Upsilon_{\odot,V}$)	$\log M_*^3$ (M_{\odot})	c_{vir}^4	$\log M_{\text{vir}}^5$ (M_{\odot})	f_{vir}^6	$f_{\text{DM},5}^7$	$\Upsilon(R_e)^8$ ($\Upsilon_{\odot,V}$)	Υ_{B5}^9 ($\Upsilon_{\odot,V}$)	$\Upsilon(R_{\text{vir}})^{10}$ ($\Upsilon_{\odot,V}$)	$\nabla_{\ell} \Upsilon^{11}$	χ^2 / d.o.f. ¹²
No-DM model												
star iso	0	7.5	11.76	–	11.76	0	0	7.5	7.5	7.5	0	123/36
NFW model												
NFW iso	0	6.4	11.69	9^{+8}_{-5}	$13.4^{+0.4}_{-0.3}$	54^{+81}_{-36}	$0.7^{+0.7}_{-0.4}$	8^{+2}_{-1}	22^{+14}_{-8}	350	0.47	28/45
NFW iso2	0	5.5	11.62	12^{+11}_{-6}	$13.3^{+0.3}_{-0.5}$	51^{+82}_{-34}	$0.8^{+0.9}_{-0.4}$	7^{+2}_{-1}	23^{+18}_{-10}	286	0.65	78/40
NFW+ β_0	0.2 ± 0.1	5.5	11.62	13^{+10}_{-6}	$13.3^{+0.3}_{-0.4}$	53^{+59}_{-32}	$0.8^{+0.7}_{-0.4}$	8^{+2}_{-1}	25^{+14}_{-10}	294	0.72	23/44
NFW+ $\beta(r)$	0.01 ± 0.1	5.7	11.64	14^{+17}_{-8}	$13.1^{+0.5}_{-0.6}$	32^{+73}_{-25}	$0.7^{+0.5}_{-0.4}$	8^{+3}_{-2}	22^{+22}_{-11}	183	0.59	12/33
NFW+AC+iso	0	5.7	11.64	8^{+8}_{-5}	$13.3^{+0.4}_{-0.6}$	45^{+40}_{-25}	$0.7^{+0.1}_{-0.3}$	7^{+1}_{-1}	17^{+10}_{-10}	261	0.39	31/44
NFW+AC+ β_0	0.30 ± 0.15	5.5	11.62	22^{+17}_{-10}	$13.2^{+0.5}_{-0.4}$	39^{+43}_{-24}	$0.8^{+1.0}_{-0.5}$	10^{+2}_{-2}	32^{+18}_{-14}	217	1.0	40/44
NFW+AC+ $\beta(r)$	0.01 ± 0.1	5.5	11.62	$7.5^{+4.0}_{-3.0}$	$13.4^{+0.3}_{-0.4}$	66^{+50}_{-37}	$0.7^{+0.4}_{-0.3}$	7^{+1}_{-1}	18^{+8}_{-6}	368	0.44	15/33
LOG model												
Model	β_5^1	Υ_*^2 ($\Upsilon_{\odot,V}$)	$\log M_*^3$ (M_{\odot})	v_0^{13} (kms^{-1})	$\log M_{\text{vir}}^5$ (M_{\odot})	r_0^{14} (arcsec)	$f_{\text{DM},5}^7$	$\Upsilon(R_e)^8$ ($\Upsilon_{\odot,V}$)	Υ_{B5}^9 ($\Upsilon_{\odot,V}$)	$\Upsilon(R_{\text{vir}})^{10}$ ($\Upsilon_{\odot,V}$)	$\nabla_{\ell} \Upsilon^{11}$	χ^2 / d.o.f. ¹²
LOG iso	0	6.6	11.70	456	$13.66^{+0.07}_{-0.08}$	251	$0.73^{+0.05}_{-0.06}$	$7.5^{+0.5}_{-0.3}$	25^{+6}_{-5}	600	0.57	25/45
LOG+ β_0	$0.3^{+0.1}_{-0.3}$	5.5	11.63	425	$13.55^{+0.12}_{-0.08}$	190	$0.77^{+0.06}_{-0.06}$	$6.7^{+1.3}_{-0.6}$	24^{+8}_{-5}	485	0.73	27/44
LOG+ $\beta(r)$	0.01 ± 0.1	6.0	11.66	412	$13.52^{+0.08}_{-0.09}$	173	$0.75^{+0.04}_{-0.05}$	$7.4^{+0.8}_{-0.5}$	24^{+5}_{-4}	440	0.65	19/33
LOG+AC+iso	0	6.3	11.67	443	$13.62^{+0.14}_{-0.13}$	362	$0.67^{+0.11}_{-0.17}$	$6.6^{+0.7}_{-0.3}$	19^{+11}_{-6}	540	0.39	21/44
LOG+AC+ β_0	$0.3^{+0.1}_{-0.3}$	5.5	11.62	419	$13.54^{+0.10}_{-0.07}$	182	$0.77^{+0.05}_{-0.05}$	$6.9^{+1.2}_{-0.6}$	24^{+7}_{-4}	465	0.72	28/44
LOG+AC+ $\beta(r)$	0.01 ± 0.1	5.5	11.62	403	$13.48^{+0.12}_{-0.09}$	290	$0.70^{+0.07}_{-0.08}$	$6.0^{+0.4}_{-0.2}$	18^{+6}_{-4}	414	0.47	21/33

NOTES: 1) Anisotropy at the benchmark radius of $5 R_e$; 2) dynamical stellar mass-to-light ratio M/L , in B -band Solar units; typical uncertainty is $\pm 0.2 \Upsilon_{\odot,V}$; 3) log of stellar mass in solar units (uncertainties are of the order of 0.1 dex); 4) concentration parameter (see §3.2.1); 5) log of virial dark mass; 6) ratio of total dark and luminous matter within the virial radius, $f_{\text{vir}} = M_d/M_*$ at r_{vir} ; 7) dark matter fraction, $f_{\text{DM}} = M_d/(M_d + M_*)$ at $5 R_e$; 8) dynamical M/L at R_e ; 9) dynamical M/L at $5 R_e$; 10) dynamical M/L at the virial radius (uncertainties are of the order of 50–70%); 11) M/L logarithmic gradient; 12) χ^2 statistic (see text for details of data included); 13) asymptotic circular velocity (see Fig. 10 for uncertainties); 14) halo core radius (see Fig. 10 for uncertainties).

more consistent with a Salpeter IMF than with Kroupa (to be addressed further in §3.5.1).

The central NFW halo parameters of $\rho_s = 0.0030^{+0.0012}_{-0.0009} M_{\odot} \text{pc}^{-3}$ and $r_s = 915'' \pm 200'' = 76 \pm 17$ kpc (see Fig. 7 which shows the joint region of permitted values for r_s and ρ_s , marginalized over the other free parameters, Υ_*) correspond to a virial radius, mass, and concentration of $r_{\text{vir}} = 770 \pm 70$ kpc, $M_{\text{vir}} = (2.5^{+3.8}_{-1.7}) \times 10^{13} M_{\odot}$ and $c_{\text{vir}} \sim 9^{+8}_{-5}$. These halo parameters are comfortably compatible with WMAP5 expectations (Eqs. 12 and 13), as well as WMAP1 (modulo an IMF issue that we discuss below). Looking carefully at the details of the DM halo solution, the VD (kurtosis) data within $20''$ – $100''$ (1.3–2 dex) are slightly overestimated (underestimated) by the model, which might be either an indication of 1) some degree of anisotropy or of 2) a mass excess caused by a larger DM concentration not accounted for in the NFW halo model.

Before we explore these two options, we will investigate further the IMF issue mentioned above.

In the NFW dark halo model solutions discussed so far, the best-fit Υ_* (~ 6.4) is more comfortably consistent with the stellar M/L predicted by the population analysis assuming a Salpeter IMF than a Kroupa IMF (see §3.1). Although this is not a strong argument for preferring either IMF, we have tried to quantify the effect of Υ_* on our result.

The high Υ_* is mainly driven by the fit to the central data-points and the tendency of the χ^2 procedure to favour more minimal halo solutions. Since our simple Jeans models are not designed to reproduce detailed kinematical struc-

ture as might be present in the central regions, we lower the weight of the very central VD and kurtosis data-points (i.e. data up to $30''$, ~ 1.5 dex) in the χ^2 minimization. In this case, more centrally concentrated halo solutions can be made compatible with the data¹⁴. Indeed, in Fig. 7 (thin purple dashed line), we report the best fit obtained for the isotropic assumption, where a lower stellar M/L is needed, $\Upsilon_* = 5.5$, which implies a dark matter halo with $\rho_s = 0.0049^{+0.0021}_{-0.0013} M_{\odot} \text{pc}^{-3}$ and $r_s = 720'' \pm 200'' = 60 \pm 17$ kpc corresponding to a virial radius, mass and concentration of $r_{\text{vir}} = 720 \pm 30$ kpc, $M_{\text{vir}} \sim 2.1 \times 10^{13} M_{\odot}$ and $c_{\text{vir}} \sim 12$ (see also “NFW iso2” solution in Table 2). In this case, though, the halo concentration is higher than predicted for WMAP5 parameters.

In Fig. 7 it is evident that this solution has a shallow velocity dispersion profile at $R < 25'' \sim 1.4$ dex which is a poor match to the data and causes the high χ^2 value for the fit. However, the gap can be filled either with the presence of some (anticipated) degree of anisotropy in the central regions or by a DM enhancement by an adiabatically contracted halo. In the following, we will explore these two possibilities in turn.

¹⁴ E.g., in Fig. 5 of §3.1 a lower central M/L is found (though for the $\beta = +0.5$ case).

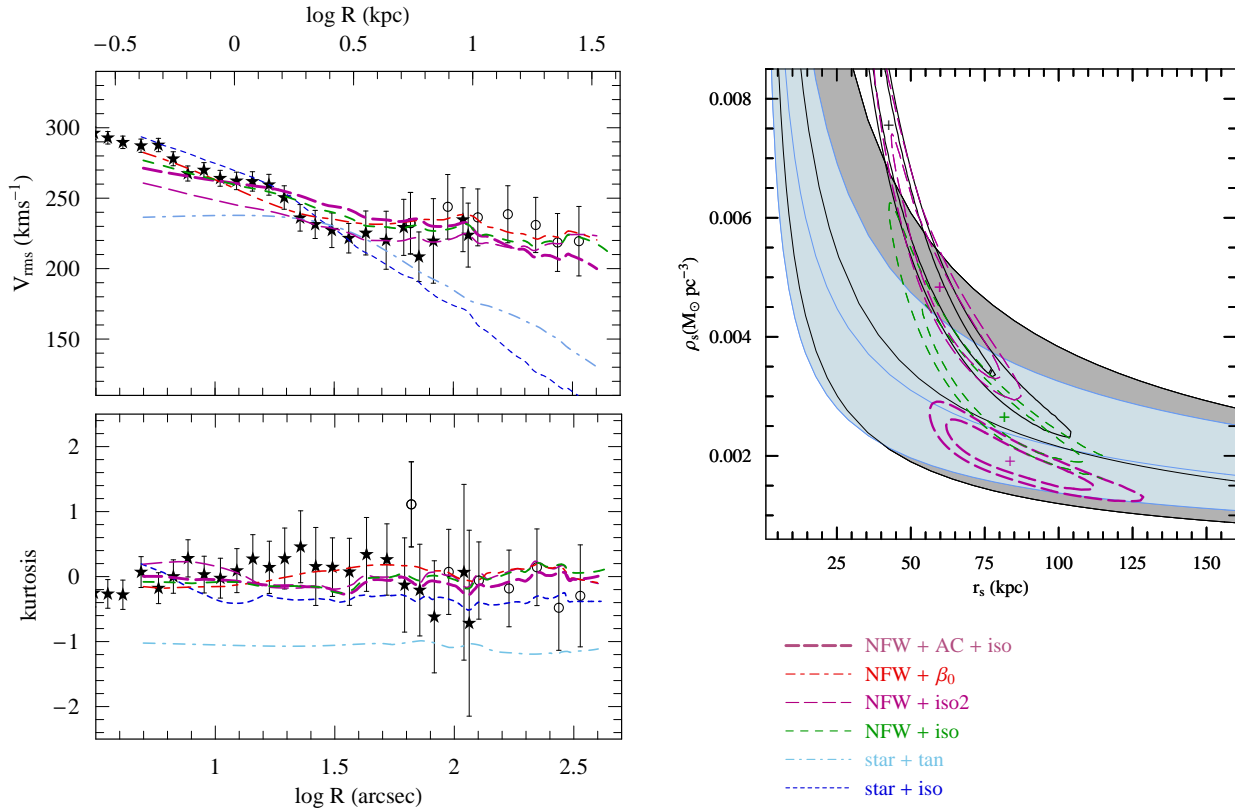


Figure 7. Multi-component Jeans model fits to the NGC 4374 kinematics data. The stellar data are shown by star symbols, and the PN data are open circles. The left panels show the projected RMS velocity profiles (top) and the projected kurtosis (bottom), the right panel the corresponding 1 and 2 σ confidence level of the $\rho_s - r_s$ parameters marginalized with respect to Υ_* and r_a (for the “NFW+ $\beta(r)$ ” model). The curves correspond to models as in the panel legend (except “star+tan” which is not a best-fit model). The shaded regions on the right show the WMAP1 (gray) and WMAP5 (blue) expected region for halo parameters. The “NFW + $\beta(r)$ ” model from Fig. 7 is plotted here for comparison with the isotropic case and repeated in Fig. 8. See text for details.

3.5.2 Models with orbital anisotropy

A way to produce a modelled steeper σ_{los} profile, for a given slope of the intrinsic light density profile, j_* , and velocity dispersion σ_r^2 (see e.g. Eq. 4), is with some degree of radial anisotropy (see, e.g., Dekel et al. 2005).

We have started with a constant anisotropy from the very central regions and the best-fit solution is found to accommodate a gentle radial anisotropy ($\beta_0 \sim 0.2$) with a lower stellar M/L ($= 5.5 \Upsilon_{\odot, V}$) that now agrees with a Kroupa IMF. The VD and the kurtosis are at last reproduced well at all fitted radii (Fig. 8, red dot-dashed line), which is reflected in an improved χ^2 value in Table 2 (“NFW+ β_0 ”).

The halo concentration for this solution is fairly high, and just consistent with the WMAP5 expectations at the $\sim 1\sigma$ level.

We remark here that the constant anisotropy solution provides a compromise model dispersion curve among regions which might have different orbital structures. For this reason we decided to test also the case of a radially varying $\beta(r)$ even though our dynamical procedure is not explicitly designed for this. As done in N+09, we will use the kurtosis data to constrain β in the outer regions where the anisotropy may be approximately constant.

Following the approach of §3.1 we use the $\beta(r)$ as in Eq. 6. The best-fit model is shown in Fig. 8 (black line) and the parameters are reported in Table 2 [“NFW+ $\beta(r)$ ”]. The anisotropy radius r_a turned out to be very close to the one estimated with the pseudo-inversion procedure ($r_a = 33''$). The match in the central regions is remarkably good also for the low Υ_* , while in the outer regions the model tracks the isotropic case (see left panel of Fig. 7 for a direct comparison), and the halo concentration is again somewhat on the high side (see Fig. 8, right panel).

We have also checked that outside $100''$ radial anisotropy is disfavoured: even when forcing the Υ_* to lower values (we tried different values down to $\Upsilon_* = 5$), in order to allow for more radial anisotropy, the match to the outer data, especially the kurtosis, was poor (see dashed orange line). This result is somewhat surprising since predictions from galaxy formation simulations generally show a significant degree of radial anisotropy (see e.g. ML05 and references therein), which has been confirmed by dynamical analysis in the case of a few galaxies (R+03; N+09; DL+09; but see Forestell & Gebhardt 2010). Indeed, we have used directly the ML05 expression (see Eq. 5) in modelling our data and found that the fit to both the VD and the kurtosis was possible only with a too small r_a ($\sim 6''$),

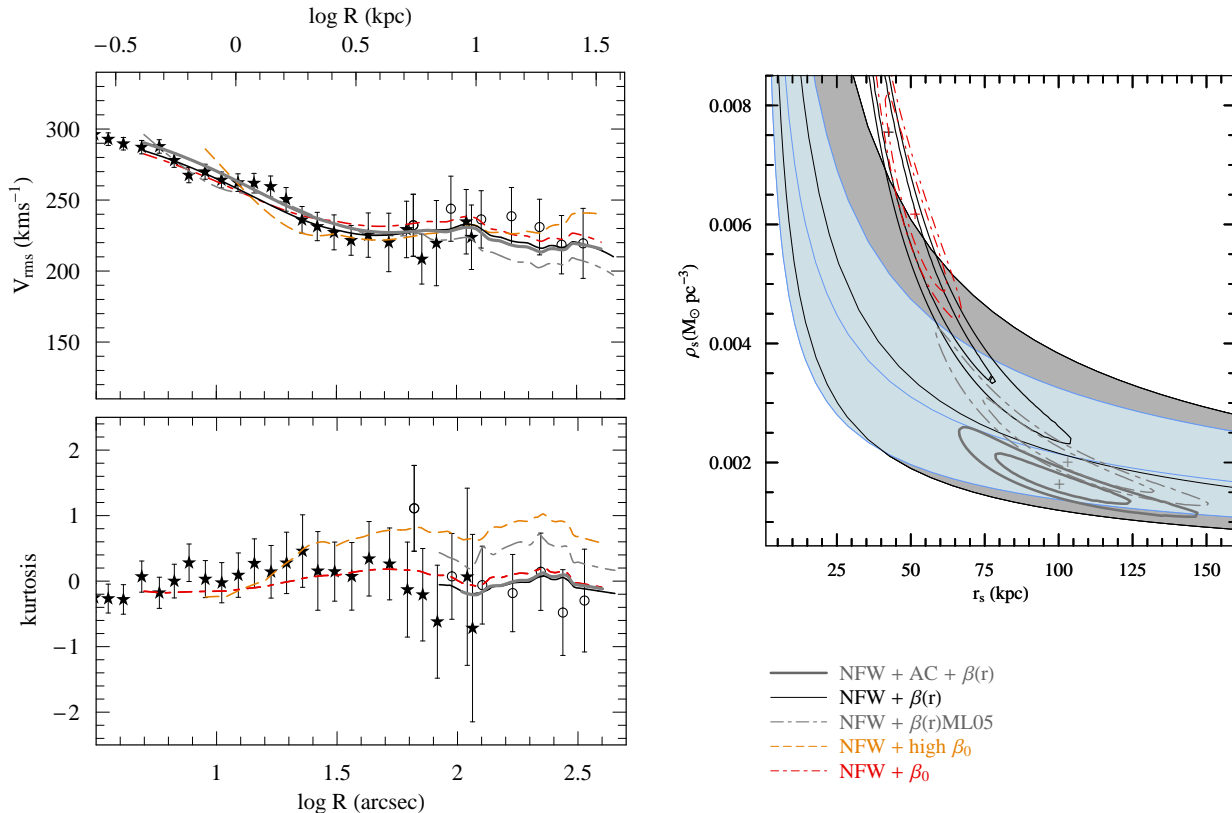


Figure 8. As Fig. 7. Confidence level of the $\rho_s - r_s$ parameters marginalized with respect to Υ_* and β_0 or r_a (except for “NFW+ high β_0 ” which is not a best-fit model). The “NFW+ $\beta(r)$ ” model is repeated as overlap with Fig. 7 .

which is completely inconsistent with the values found by Mamon & Lokas (2005, i.e. $1.4 R_e$; see Fig. 8 gray dot-dashed line). Fixing r_a to the expected value, the fit was possible only with a larger $\Upsilon_* \sim 6.5$. In either case, though, a much poorer significance of the fit than the one given by our preferred $\beta(r)$ profile (Eq. 6) was found.

In summary, our exploration of the NFW models indicates that halo parameters corresponding to WMAP5 expectations are compatible with the data. The agreement is better for a Salpeter IMF, with the concentration becoming somewhat high for a Kroupa IMF. The near-isotropic orbital distribution that we infer is at odds with standard predictions for radial orbits. However, as discussed in the Appendix, there are some uncertainties in the classification of velocity outliers, such that we cannot yet claim the isotropy conclusion as robust.

3.5.3 Effect of adiabatic contraction

The baryonic collapse occurring during galaxy assembly is one of the physical process that can shape the central DM distribution in a way different from the predictions of the dark matter only N-body simulations. Given a dark matter halo distribution with the properties predicted by such simulations, the (collisional) collapsing gas can exert a dynamical drag on the DM particles and produce a more concentrated final DM density profile (see e.g. Blumenthal et al. 1986). The net effect is a larger central DM fraction and conse-

quently a lower stellar mass contribution (i.e. a lower Υ_*) to the total mass in the central regions (for fixed dynamical M/L and halo parameters).

This process can be described analytically by an adiabatic contraction (AC hereafter; Blumenthal et al. 1986; Gnedin et al. 2004, G+04 hereafter) of the dark halo. Since there is not yet a final consensus on the effectiveness and accuracy of the descriptions on the market (see e.g. Pedrosa et al. 2010; Duffy et al. 2010; Tissera et al. 2010), we decided to use the recipe from G+04. The G+04 model produces a weaker effect on the final DM distribution than the original Blumenthal recipe, and appears closer to the results obtained in the cosmological simulations including the baryon physics.

A critical evaluation of the baryonic processes is beyond the purpose of this analysis, where we only intend to check whether including an analytical recipe for AC in our Jeans analysis would provide a viable explanation to reconcile the estimated Υ_* derived from our analysis and the stellar population models. Furthermore, to our knowledge, the use of the AC in detailed Jeans modelling of the velocity dispersion profile of an elliptical galaxy has not been attempted before, so we consider this an interesting exercise even though the AC recipe might be not optimal.

For this purpose, in our equations the total mass generating the potential $\Phi = GM(r)/r$ is given by considering as an adiabatic invariant the quantity

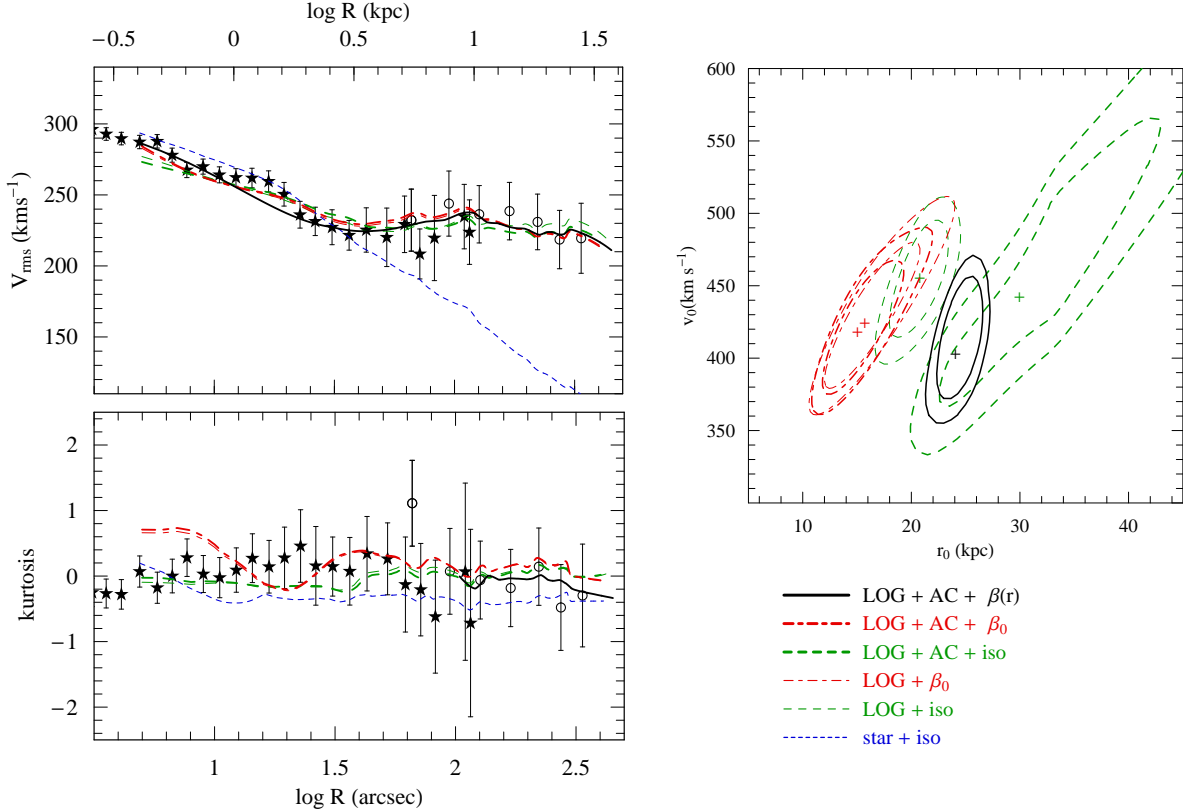


Figure 9. As Figs. 7 and 8, with LOG models. The right-hand panel shows the corresponding 1 and 2 σ confidence level of the $v_0 - r_0$ parameters marginalized with respect to Υ_* and β parameters (when available). The curves correspond to models as in the panel legends. See text for details.

$$M(\bar{r})r = \text{const} \quad (18)$$

where $\bar{x} = Ax^w$ and $x = r/r_{\text{vir}}$. By calibrating Eq. 18 to collisional N-body simulations, G+04 have fixed $A = 0.85$ and $w = 0.8$. The contracted DM mass distribution has been derived by solving the equation

$$[M_{\text{tot}}(\bar{r})]r = [M_{\text{DM}}(\bar{r}) + M_*(r_f)]r_f \quad (19)$$

where $M_{\text{tot}} = M_{\text{DM}} + M_*$, and M_{DM} and M_* are the final dark and stellar mass respectively (initially assumed to have the same spatial distribution). The model results are shown in Fig. 8 and the model parameters in Table 2 [“NFW+AC+iso, $+\beta_0$, $+\beta(r)$ ”]. There are two main remarks that we can derive from these results.

First, since the effect of the AC is to drag more DM into the central regions, the Υ_* turns out to be smaller than in the no-AC case. For the isotropic case we obtain $\Upsilon_* = 5.7 \Upsilon_{\odot,V}$ (see Fig. 7, tick purple dashed line), but if we again include $\beta(r)$ as in Eq. 6, the best fit is found for $\Upsilon_* = 5.5 \Upsilon_{\odot,V}$ and $r_a = 33''$. The goodness of these fits is slightly worse than, but similar to, the uncontracted NFW models (see Table 2) with the model curves looking very similar to the eye (see Fig. 8, tick gray line)¹⁵.

Second, the (pre-contraction) dark halo parameters

turn out to be in very good agreement with Λ CDM. E.g., for the anisotropic model, the NFW dark halo turns out to have $c_{\text{vir}} = 7.5$ which matches the WMAP5 expectation ($c_{\text{WMAP5}} \sim 7$ for $\log M_{\text{vir}} = 13.4$).

When forcing the fit to a lower $\Upsilon_* = 5 \Upsilon_{\odot,V}$, the halo parameters change slightly: the best fit is $c_{\text{vir}} \sim 9.1$ and $\log M_{\text{vir}} = 13.5$, which is higher than the typical prediction but still consistent with the scatter.

This is one of the most notable results of this paper: for the first time using stellar kinematics extended out to $\sim 5 R_e$, it has been demonstrated that the dark matter content of a giant elliptical galaxy may be compatible with Λ CDM.

3.6 Multi-component model results: LOG model

We next carry out the model sequence for the LOG mass model (Section 3.2.2), with results shown in Fig. 9 and Table 2.

3.6.1 The isotropic model

For the isotropic case, the LOG model can fit the data better than the NFW model in the central regions and equivalently well in the outer regions (see Fig. 9, thin green dashed line). This is because the LOG potential has an internal core with little DM contribution in the central regions. In this case we

¹⁵ The model with constant anisotropy and AC yielded a relatively poor fit, and a very high halo concentration (Table 2).

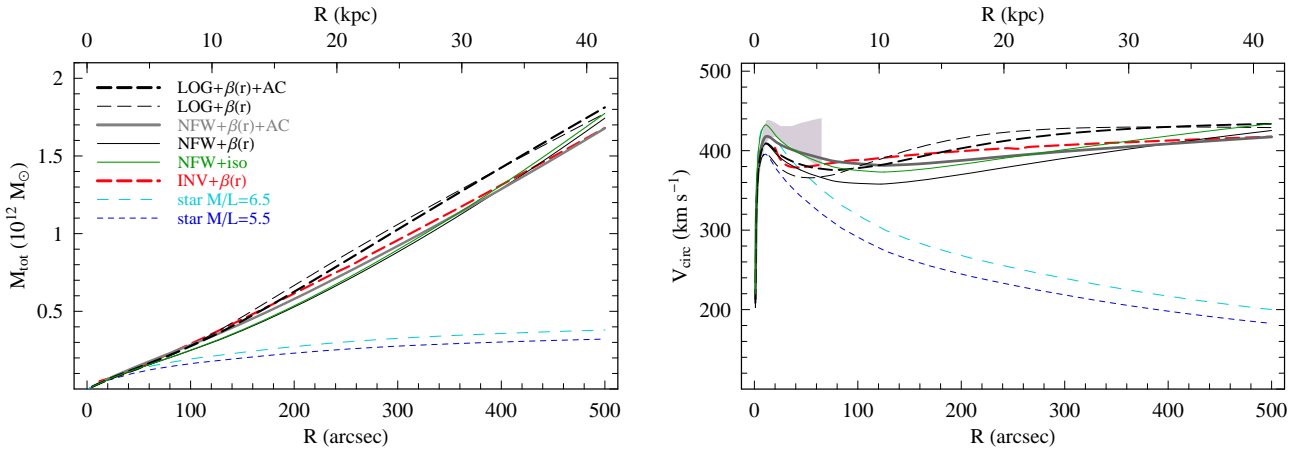


Figure 10. Radial mass distribution of NGC 4374. The left panel shows the cumulative mass, and the right panel shows the circular velocity profile. Model curves from this work are as in the legend. We also show the v_c profile from Kronawitter et al. (2000) (shaded area includes the variance of their models).

find also a large stellar mass-to-light ratio, $\Upsilon_* = 6.6 \Upsilon_{\odot, V}$, which is more compatible with a Salpeter IMF than Kroupa. A massive DM halo is required outside $\sim 100''$ (mean $v_0 \sim 450 \text{ km s}^{-1}$; see Table 2, “LOG iso”), consistently with the pseudo-mass inversion analysis and the NFW solution (see Fig. 10).

3.6.2 Models with orbital anisotropy

Adopting a constant non-zero anisotropy ($\beta_0 = 0.3$) allows for a Kroupa-compatible $\Upsilon_* = 5.5 \Upsilon_{\odot, V}$ (the same as found using the NFW+AC model). However, the fit is poorer (see Table 2, “LOG+ β_0 ”), in particular at very small radii (even though these are penalized in our model) and owing to the higher estimates of the kurtosis at $R > 100'' (=2 \text{ dex})$, as shown in Fig. 9 (thin red dot-dashed line).

We have checked if larger β_0 could be consistent with the data at large radii and found that once M/L_* and r_c are fixed, there is a degeneracy between the v_c and the β_0 values: a reasonable fit to the data is obtained for $v_c = 410 \text{ km s}^{-1}$ and $\beta_0 = 0.1$ and $v_c = 470 \text{ km s}^{-1}$ and $\beta_0 = 0.5$ with $M/L_* = 6 \Upsilon_{\odot, V}$ and $r_c = 25 \text{ kpc}$. Once again, the kurtosis helps to put constraints on the allowed β_0 : the $\chi^2/\text{d.o.f.}$ calculated over only the model versus observed kurtosis profiles is much smaller for $\beta_0 = 0.1$ ($\sim 9/20$) than for $\beta_0 = 0.3$ ($\sim 12/20$) and $\beta_0 = 0.5$ ($\sim 22/20$), which is a final demonstration that strong anisotropy can be excluded at large radii.

Finally, we have adopted the $\beta(r)$ as in Eq. 6. The best-fit model is not showed (but almost identical to the one with AC as in §3.6.3), while parameters are reported in Table 2 [“LOG+ $\beta(r)$ ”]. The anisotropy radius r_a is slightly larger than the one estimated with the pseudo-inversion procedure and NFW ($r_a = 45''$), although the $\beta(r)$ profile turns out to be almost unaltered. The $\Upsilon_* = 6 \Upsilon_{\odot, V}$ is closer to the isotropic case, since this is mainly constrained by the central regions which are almost isotropic according to the Eq. 6.

3.6.3 Adiabatic Contraction

For completeness, we have modelled the effects of a hypothetical AC on the LOG halo. Because of the non-cuspy nature of the initial halo, AC turns out to have only a weak affect, and does not change any of the above conclusions. Model curves are almost indistinguishable from the ones with no-AC as shown in Fig. 9 (green thick dashed line: isotropy; red thick dot-dashed line: constant anisotropy) as a consequence of best-fit parameters very close to the ones obtained for no-AC [Table 2 “LOG+AC+iso, + β_0 , + $\beta(r)$ ”, and confidence contours in Fig. 9].

Finally, the simultaneous use of the $\beta(r)$ anisotropy as in Eq. 6 and the AC allowed the best fit to the data (black thick line) as for the NFW case. For the LOG potential the stellar M/L turned out to be $\Upsilon_* = 5.5 \Upsilon_{\odot, V}$ and $v_0 = 403 \text{ km s}^{-1}$ (see Table 2), and the anisotropy radius turned out to be very similar to the NFW models ($r_a = 35''$). Once again the AC seemed to be a crucial ingredient to alleviate the problem of the stellar M/L problem by naturally accommodating a Kroupa-like Υ_* .

3.7 Summarizing the best halo models: mass profiles and circular velocities

Before we discuss the implications of the best-fit solutions from the previous sections, we summarize the models which we consider more physically meaningful. As seen in Table 2 and discussed earlier, most of the models presented are statistically good fits (e.g. the reduced $\tilde{\chi}^2 = \chi^2/\text{d.o.f.}$ is almost everywhere < 1), but some of the models were incompatible with related theoretical predictions.

For instance, the no-AC models “NFW+ β_0 ” and “NFW+ $\beta(r)$ ” have $\tilde{\chi}^2 = 0.5, 0.4$ respectively, but the implied halo concentrations are improbable given the ΛCDM expectations. Also “NFW+iso” has a rather small $\tilde{\chi}^2 = 0.6$ and a fairly ΛCDM -like halo, but the large Salpeter-like $\Upsilon_{\odot, V}$ makes this solution unfavourable. On the other hand the model “NFW+AC+ $\beta(r)$ ” has a $\tilde{\chi}^2 = 0.45$ and is fully consistent with both ΛCDM concentrations and a Kroupa IMF, and so is considered our best reference

model. For similar reasons, the favoured LOG models are the “LOG+AC+ $\beta(r)$ ”, “LOG+ β_0 ” and “LOG+AC+ β_0 ”—all having $\chi^2 \sim 0.65$ and a $\Upsilon_{\odot, V}$ compatible with a Kroupa IMF.

Going to the comparison among the different potentials compatible with the stellar kinematics, in Fig. 10 we plot the mass profiles of some of these model solutions in order to gain a general sense of the different halo solutions accommodated by the data.

Considering the mass profiles, $M(r)$, for the different models discussed above, the DM halo models (NFW and LOG) are very different from the no-DM case, with the v_c remaining much flatter with radius than the stellar model.

The mass profile at $5 R_e$ (~ 30 kpc) is remarkably similar for the NFW and LOG models, demonstrating that this quantity is well constrained by the data, independently of the details of the mass models.

Despite the uncertainties, for the NFW case the mass profiles as well as the v_{circ} profiles differ in the very central regions when comparing the un-contracted solutions and the contracted haloes. The relative normalization between the stellar and halo masses changes due to the higher dark mass allowed by the AC for a given halo concentration before the contraction. For the LOG model, Υ_* seems to be more degenerate with the β value in the central regions (in the sense that higher β would allow smaller Υ_* , see §3.2.2). Overall, the v_{circ} profiles (Fig. 10) turn out to be fairly similar among the different models up to the last datapoint ($\sim 340''$), and beyond, if the profiles are extrapolated more deeply into the halo regions. Furthermore, the mass profiles are remarkably similar to the results of the pseudo-inversion method (see Fig. 5).

Finally, in Fig. 10 we compare our results with the v_{circ} profile from K+00, which is based on long-slit data extending out to $\sim 70''$. Focusing on our LOG+ $\beta(r)$ solution which is the most equivalent to theirs, our results are identical in the very central regions, with a slight discrepancy at larger radii. Note that the v_{circ} from K+00 extrapolated to $300''$ (Fig.17 in Gerhard et al. 2001) is significantly lower than our new profile based on more extended data and models.

The asymptotic run of all the model curves in Fig. 10 is remarkably tight which means that at intermediate scales (of the order of the r_s scale of the NFW haloes) the overall galaxy mass is quite well constrained and the scatter introduced by the halo models and the allowed anisotropy is small. However, an important cross-check would be to verify how these models might differ around the virial radius, where the NFW and LOG profiles are expected to differ significantly (although the extrapolated M_{vir} values in Table 2 do not differ much).

4 DISCUSSION

The dynamical solutions for the bright elliptical NGC 4374 all clearly indicate that this galaxy is surrounded by a massive DM halo. DM haloes were also found in four ordinary ETGs studied using PNe (not all of these studies using PN constraints): NGC 3379 (R+03; DL+09; Weijmans et al. 2009); NGC 4697 (DL+08); NGC 4494 (N+09; Rodionov & Athanassoula 2010); NGC 821 (Weijmans et al. 2009; Forestell & Gebhardt 2010). Apart

from alternative gravity theories (e.g. Tiret et al. 2007), it seems clear that elliptical galaxies in general contain DM, and the question is how the DM profiles compare in detail to predictions.

Some of the galaxies above were modelled with NFW haloes and some with LOG haloes, while NGC 4374 is the first of these cases where *both* were tried. Unfortunately, we were not able to discriminate between the two models, given the limitations of the simple Jeans approach which cannot fit the observations in great detail and requires somewhat arbitrary weighting of the data points. Interestingly, the two models do seem to prefer different Υ_* values, corresponding to Kroupa and Salpeter IMFs for the NFW and LOG haloes, respectively. Adopting a prior on the IMF may then provide more information about the DM profile, and vice-versa. More detailed modelling may also be able to discriminate between these haloes on the basis of dynamics alone: e.g. with much less extensive data in a sample of ETGs, but using Schwarzschild modelling, Thomas et al. (2007) found some suggestions that LOG haloes were preferred over NFW.

Adopting the NFW halo model for the time being, it is important to test the inferred halo parameters (density and scale-length, or virial mass and concentration) against predictions from cosmological simulations. N+09 assembled the PN-based results as well as a heterogeneous sample of other mass results from the literature. We reproduce this mass-concentration plot in Fig. 11, with the theoretical prediction updated for the WMAP5 cosmological parameters.

Although the mass profile uncertainties for any single galaxy are too large to make definitive statements, when considering a handful of galaxies together, a remarkable pattern begins to emerge. The fast-rotator or ordinary ETGs (along with spiral galaxies) appear to have low concentration haloes, and the slow rotators to have high concentrations, with a possible zone of avoidance in between, corresponding to the theoretical predictions. With the shift to WMAP5 predictions, the low concentrations become *less* of a problem, and the high concentrations *more*.

Adding NGC 4374 to the diagram confirms this picture with a PN-based slow rotator analysis for the first time. The NFW solution with a standard Kroupa IMF coincides with the high-concentration region previously found for slow rotators using somewhat similar analyses. However, the story changes with certain modifications to the models. If the IMF is forced to Salpeter, less central DM is permitted and the implied concentration decreases. Alternatively, the high central DM content could be due to AC, with the “original” concentration much lower, as illustrated by the modelling. In either of these cases, the halo concentration becomes consistent with Λ CDM predictions.

Selecting a “heavy” IMF or including AC may thus generally solve the concentration crisis for slow rotators—but what about the fast rotators? Although we have not explicitly modelled these galaxies with AC, some general trends may be gleaned from the Λ CDM-based toy models of Napolitano, Romanowsky & Tortora (2010). Their Figs. 6 and 11 illustrate that for ETGs of all masses, AC is expected to dramatically increase the fraction of DM found in the central R_e . This implies that if AC were included in the models of the fast rotators of Fig. 11, the halo concentrations which are currently on the margin of consistency with theory would become problematically low.

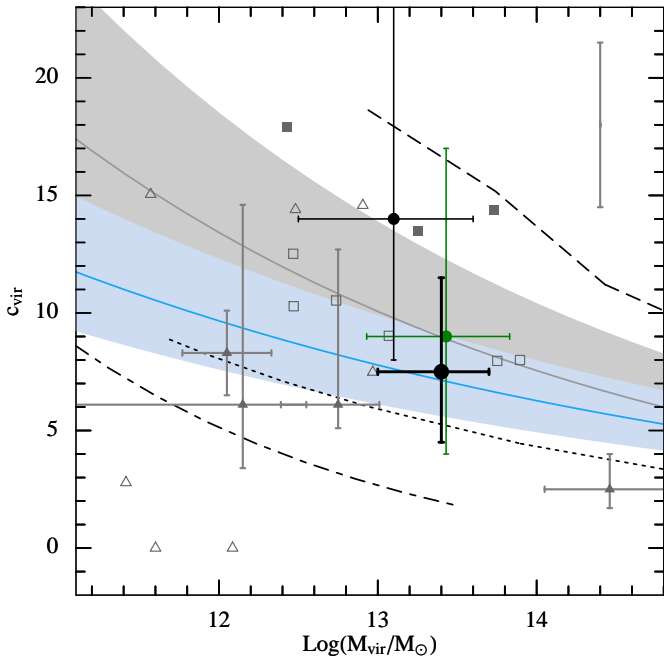


Figure 11. Dark matter halo virial mass and concentration parameters. Several reference solutions for NGC 4374 (*large filled circles*) are plotted as well as other data taken from N+09. The blue and gray curves with surrounding shaded regions are the WMAP5 and WMAP1 predictions, respectively. The green small dot with error bars is the “NFW iso” solution (see Table 2; the stellar M/L is consistent with a Salpeter IMF), the black small dot is “NFW+ $\beta(r)$ ” (corresponding to a Kroupa IMF), and the big black dot is to our favoured model “NFW+AC+ $\beta(r)$ ”. From N+09: *Triangles* and *boxes* mark fast-rotator and slow-rotator ETGs, respectively. The *small filled symbols* mark detailed ETG dynamical results using PNe and GCs (including error bars, where available). The *open symbols* show the dynamics-based ETG results from N+05, with error bars in the upper right corner showing the typical uncertainties. The *dashed line* shows the mean result for X-ray bright groups and clusters, the *dot-dashed curve* is an inference for late-type galaxies, and the *dotted curve* is the trend from weak lensing of all types of galaxies and groups (see N+09 for details).

An alternative scenario might be to adjust the IMFs of the fast rotators to be *lighter* than Kroupa (Salpeter is incidentally too heavy in general for this class of galaxies; cf. C+06). This would allow for more central DM and conceivably increase the inferred concentrations.

In order to move all the “observed” ETG halo concentrations into reasonable agreement with the predictions, we arrive at the tentative solution that (1) the slow rotators have Salpeter IMFs or AC, *and* (2) the fast rotators have ultra-light IMFs or no AC. If (1) and (2) are fulfilled, then there may still be a systematic concentration offset between fast and slow rotators, but this would be small enough to be plausibly explained by differing collapse redshifts.

This solution would present the very interesting possibility that the fast and slow rotators are dramatically different in either their IMFs or their halo contraction histories. Systematic transitions in these properties have been suggested for various reasons in the past, but they appear to go in the wrong direction. In the modern “downsizing” picture

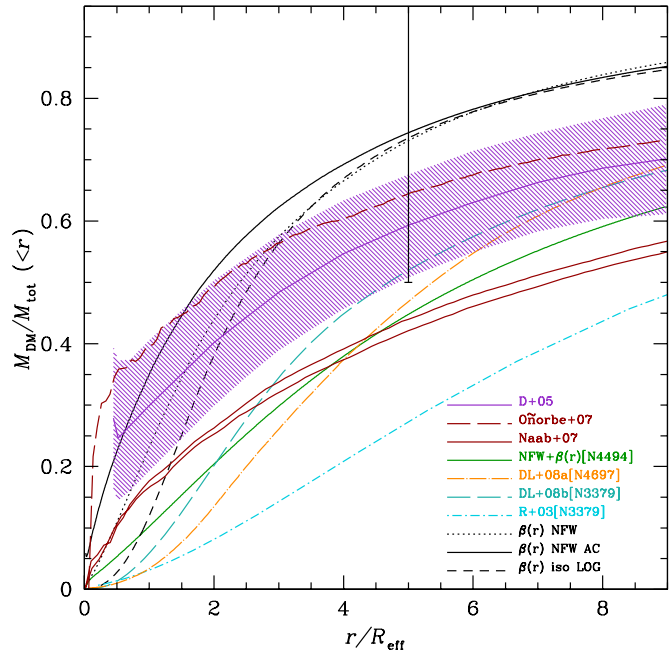


Figure 12. Cumulative dark matter fraction as a function of radius. Results for different observed and simulated galaxies are indicated with different colours and line styles as in the legend, with the results for NGC 4374 in black. The errorbar marks the typical error for the dark matter fraction of NGC 4374 at $5 R_e$.

of galaxy formation (e.g., Nelan et al. 2005; Thomas et al. 2005; Cimatti et al. 2006; Pannella et al. 2006; Graves et al. 2007; Calura et al. 2008), the more massive galaxies like NGC 4374 would have on average formed their stars earlier and more rapidly than in the more ordinary ellipticals. As summarized by Napolitano, Romanowsky & Tortora (2010, Sec. 4.4), the IMF in these conditions is thought to have been if anything *lighter* rather than heavier.

Also, as summarized in N+09, it is thought that AC could be counteracted by rapid, clumpy and starburst assembly histories, while AC classically implies smooth, slow gaseous infall (see also Lackner & Ostriker 2010). These conditions would suggest that the *spirals* should have stronger AC, and galaxies like NGC 4374 should have weaker AC (a point also made by Chen & McGaugh 2008).

Returning to a less model-dependent view of the mass profiles, we plot the cumulative DM fraction versus radius in Fig. 12, as also done in N+09. The model inferences for NGC 4374 as well as some of the ordinary ETGs are plotted, along with examples from galaxy formation simulations (both in a full cosmological context and using ad-hoc mergers; Dekel et al. 2005; Naab et al. 2007; Oñorbe et al. 2007). Drawing attention to the $5 R_e$ reference value, we see that the DM fraction for NGC 4374 of ~ 0.7 – 0.8 is significantly larger than what was found so far for ordinary ellipticals (~ 0.4 – 0.5), and similar to what has been found for group- and cluster-central ellipticals (~ 0.8 – 0.9 using X-ray rather than dynamical methods; Das et al. 2010). These results bracket the simulations values of ~ 0.5 – 0.6 .

The DM fraction results within $1 R_e$ in Fig. 12 based on detailed dynamical modelling at first glance do not seem to

square with other recent results from the literature. Various combinations of dynamical, strong gravitational lensing, and stellar populations analyses have found typical DM fractions within $1 R_e$ of ~ 0.4 for fainter ellipticals and ~ 0.6 for brighter ones (Napolitano, Romanowsky & Tortora 2010; Schulz et al. 2010; Tortora et al. 2010b; Auger et al. 2010), versus ~ 0.05 and ~ 0.3 here.

However, in the case of NGC 4374, the ambiguity in the R_e comes into play. In NRT10, galaxies of the same stellar mass have $R_e \sim 12$ kpc on average, or $\sim 145''$ at the distance of NGC 4374. Using this R_e scale, we would have a DM fraction of ~ 0.5 , consistent with the literature. As for the lower-luminosity ellipticals, NRT10 did find a fraction of galaxies (particularly ones with older stars) to have DM fractions lower than ~ 0.1 , so the critical goal is to assemble a large sample of galaxies with detailed dynamical models to establish the trends with good statistics. Fig. 1 of Trujillo-Gómez et al. (2010) does suggest that these three galaxies may happen to represent one extreme from a broad distribution of DM properties at intermediate luminosities. If this situation is true, the arguments above about halo concentration offsets would no longer apply.

5 CONCLUSIONS

We have presented a full Jeans analysis of the bright, slow-rotator elliptical NGC 4374 based on the observations of ~ 450 PNe with the Planetary Nebula Spectrograph. The PN line-of-sight velocities extend out to $\sim 5 R_e$. We have constructed spherical Jeans dynamical models of the system: a “pseudo-inversion” model and multi-component mass models with and fourth-order moments constraints on the orbital anisotropy.

The two approaches return similar values of M/L and anisotropy (see Fig. 5 and Table 2) and both imply that NGC 4374 is a very dark matter dominated system with a near-isotropic orbital distribution in its halo. Dynamical analyses of more ordinary ETGs have suggested radially-biased anisotropy in their haloes as predicted by simulations (see Section 3.5.2). The NGC 4374 result on the other hand would build on previous suggestions that slow rotators have surprisingly isotropic haloes, which would suggest a new scenario for building of the extended stellar envelopes of these galaxies may be required (Hwang et al. 2008; Romanowsky et al. 2009). However, in this case the anisotropy result is sensitive to the assumptions about outlier velocities, and further investigation is required.

The mass profile results are on the other hand fairly insensitive to the outliers. The high DM fraction inferred within $\sim 5 R_e$ confirms the apparent dichotomy in DM content between slow and fast rotators proposed by N+09 (see also Bertin et al. 1994; C+06; Napolitano et al. 2008; C+09), and yields two important implications: (1) the DM dichotomy is not a result of systematic differences in the mass tracers used; (2) it is not a simple difference of group-central versus satellite galaxies since NGC 4374 does not appear to be at a group center (while the low-DM system NGC 3379 is).

This apparent DM bimodality may mirror other transitions in ETG properties at similar luminosity scales, such as the relations between size and mass (e.g. Shen et al.

2003; Tortora et al. 2009), size and surface brightness (e.g. Capaccioli et al. 1992), luminosity and velocity dispersion (Faber & Jackson 1976) and the colour/population properties (Tortora et al. 2010a).

Given the limitations of the Jeans models and the stellar/dark mass degeneracy, we are not able to distinguish between different DM radial profiles, including LOG, NFW and NFW+AC haloes. The LOG models prefer high stellar masses consistent with a Salpeter IMF, NFW works with either Salpeter or Kroupa, and NFW+AC requires Kroupa. The nominal NFW+Kroupa model implies a halo with a concentration that is somewhat high, given WMAP5-based predictions. Adopting either Salpeter IMF or AC brings the inferred concentration down to the expected value. Thus, considering that AC has commonly been considered the default expectation in galaxy formation, we have finally found an ETG analyzed using PNe that is naturally consistent with theoretical expectations for the DM halo.

Comparing the NFW halo parameters obtained for NGC 4374 as well as for an assortment of other galaxies in the literature, we find evidence for the slow rotators to have much higher halo concentrations on average than the fast rotators. We discuss some possible variations in IMF and AC which could explain this difference, but there are also suggestions that the sample of fast rotator galaxies is a statistical fluke.

Two primary avenues are needed to make further headway in pinning down the properties of DM haloes in ETGs. One is to carry out more detailed dynamical and stellar populations modelling in an attempt to discern the DM profiles in detail. The other is to expand the sample of galaxies studied, particularly at intermediate luminosities ($M_B \sim -20$). Work on both fronts is underway as part of the PN.S Elliptical Galaxy Survey.

ACKNOWLEDGMENTS

We would like to thank the anonymous referee for the fast report and useful suggestions, and Isaac Newton Group staff on La Palma for supporting the PN.S over the years. We also thank Crescenzo Tortora for stimulating discussions. AJR was supported by the National Science Foundation Grants AST-0507729, AST-0808099 and AST-0909237, and by the FONDAP Center for Astrophysics CONICYT 15010003. This research has made use of the NASA/IPAC Extragalactic Database (NED) which is operated by the Jet Propulsion Laboratory, California Institute of Technology, under contract with the National Aeronautics and Space Administration. We acknowledge the usage of the HyperLeda database (<http://leda.univ-lyon1.fr>).

APPENDIX A: ALTERNATIVE OUTLIER SELECTION AND DYNAMICAL IMPLICATIONS

As discussed at the beginning of Section 2, a handful of “outlier” PNe were rejected from the overall sample using a 3σ “friendless” analysis. Although relatively few in number, the inclusion or exclusion of these objects in our dynamical

analyses could have a large impact on the conclusions, which we consider here in more detail.

Fig. 1 showed the six outliers identified through this process. Two of them are extreme outliers and can be securely rejected, but the other four are only barely excluded at 3σ . This is a concern since in a data set of 450 objects with a Gaussian velocity distribution, there should on average be one random object found past 3σ , and if a non-Gaussian distribution is allowed, then many more would be possible¹⁶.

We are not at a complete impasse since we notice that all the outliers have negative velocities relative to NGC 4374, which is not likely to be just a chance occurrence¹⁷.

We look at the situation in two-dimensions in Fig. A1, focusing on the most outlying velocities. It turns out that the four most extreme velocities lie on an axis to the East of the galaxy’s center, which is also the direction of the nearby giant elliptical NGC 4406 (M86) found $\sim 1000''$ away. A similar pattern has been found in the globular cluster system of NGC 4374 (B. Kumar et al., in prep).

The -1300 km s^{-1} relative systemic velocity of NGC 4406 (v_{rel}) provides a handy explanation for the low-velocity outliers—whether these objects simply belong to the NGC 4406 PN system seen in projection, or are part of an interaction region between the two galaxies (Arnaboldi et al. 1996).

Although a full analysis for such an interaction scenario is outside the scope of this paper, we can quantify the effect of a fly-by encounter between the two galaxies using the *impulse approximation* to estimate the energy injection into the outer galaxy envelope (see e.g. Napolitano et al. 2002). We calculate an upper limit to this energy by assuming a tangential encounter with an impact parameter of $b = 1000''$:

$$\Delta E = \frac{4GM_1M_2^2}{3b^4v_{\text{rel}}^2r^2}, \quad (\text{A1})$$

where G is the gravitational constant, $M_1 \sim 6 \times 10^{12} M_{\odot}$ (e.g., from the “NFW+iso2” model) is the mass of the perturbed system (NGC 4374) which has been calculated within the impact parameter b , $M_2 = 0.5 \times M_1$ at the same radius, and the mean square radius of NGC 4374, $\overline{r^2}$ is taken as equivalent to the square of characteristic scale of the dark matter halo ($\sim 6.4 \times 10^3\text{ kpc}^2$).

The resulting energy change is $\Delta E = 9.2 \times 10^{16} M_{\odot} \text{ km}^2 \text{ s}^{-2}$ which provides a heating contribution to the dispersion of $\sigma_{\text{heat}} = 2\Delta E/(3M_{\text{shell}})$, where M_{shell} is the mass of the galaxy shell which has experienced the energy transfer. Taking this shell in the radial range of $200''$ – $1000''$ (i.e. $\gtrsim 3 R_e$), we find $\sigma_{\text{heat}} \sim 100\text{ km s}^{-1}$.

This extra heating term could handily explain the higher dispersion on the low velocity side as implied by the

¹⁶ We have checked how the outlier velocities compare to the local escape velocities in our best-fit NFW halo (e.g. the NFW+AC+ $\beta(r)$ in Table 2), which turns out to be $\sim 1250\text{ km s}^{-1}$ relative to the systemic velocity. The two most extreme outliers would in this case not be bound to NGC 4374, but the other four could be.

¹⁷ This asymmetry does not appear to be caused by an error in the adopted value of v_{sys} , as the peak of the LOSVD coincides with our self-consistent v_{sys} , which is in turn very close to the NED value.

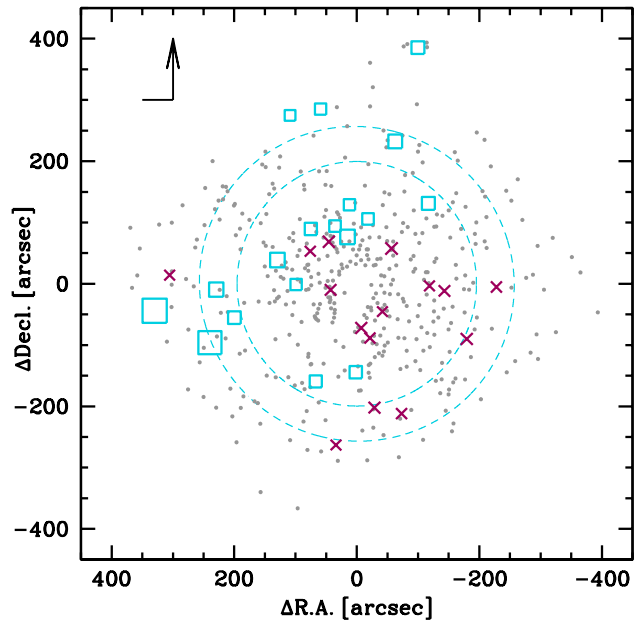


Figure A1. Diagram of potential velocity outlier PNe. The 2D positions on the sky are shown relative to the center of NGC 4374, with the stellar isophotes at $R_m = 197''$ and $257''$ show as dashed ellipses. Squares represent approaching velocities and crosses are receding velocities, with symbol size proportional to relative velocity amplitude. The ~ 30 most extreme velocity PNe are shown along with the candidate outliers, to illustrate the normal velocity field of NGC 4374. The remaining PNe are shown as small grey points. The North and East directions are shown in the top-left corner.

“outliers” in Fig. 1. In this scenario, the close passage between the galaxies would have heated the Eastern side of NGC 4374, with this event happening less than one-crossing time ago so that the asymmetry is preserved. Removing the four “outliers” would then restore the observed kinematics of the system to the approximate pre-interaction state, suitable for equilibrium dynamical analyses.

The interaction calculation above has been done under the assumption of the closest encounter (and the highest energetic) allowed by the observed geometry. Any other less favourable configuration would produce a smaller energy transfer and a more local effect of the encounter. In this case, the four Eastern low-velocity objects are likely to be true outliers, and the remaining two outliers to the North are less certain, and could be part of the normal velocity distribution of NGC 4374.

If those two objects are kept in the final sample then the velocity dispersion and kurtosis profiles are somewhat changed in the outer regions, as shown in Fig. A2. The dispersion profile becomes slightly flatter (slope -0.03 ± 0.07 instead of the -0.07 found in §2.2). The kurtosis profile rises at large radii, where if we were to again use the equation B10 approximation from N+09, we would infer a higher radial anisotropy ($\beta \sim +0.4$ instead of ~ -0.1).

Carrying out some dynamical models as in the main Sections, we show in Fig. A2 the results for the isotropic and $\beta(r)$ NFW mass models. We find best-fitting halo parameters of $\rho_s = 0.0019, 0.0030 M_{\odot} \text{ pc}^{-3}$ and $r_s = 110, 87\text{ kpc}$ re-

spectively, corresponding to $c_{\text{vir}} = 8_{-2}^{+5}, 10_{-4}^{+6}$ and $\log M_{\text{vir}} \sim 13.6M_{\odot}$. These parameters are very similar to those found using our default outlier selection (see Figs. 7 and 8), although the χ^2 fits are poorer.

We also try out a more strongly varying $\beta(r)$ function motivated by the higher kurtosis, with high radial anisotropy at larger radii as illustrated by the right-hand panel of Fig. A2 and named β_3 and β_4 some fixed profiles which bracket the tentative anisotropy value in the latest radial bin estimated as above ($\sim +0.4$). In this case the fit is performed on the dispersion curve only.

The quality of the corresponding dynamical model fit (top-left panel) is similar to the previous case, but the best-fit dark matter halo turns out to be almost identical for the two anisotropy profiles and have a higher halo concentration and small virial mass, slightly off the WMAP5- Λ CDM predictions: $\rho_s = 0.006 M_{\odot} \text{pc}^{-3}$ and $r_s = 46 \text{ kpc}$, corresponding to $c_{\text{vir}} = 13_{-6}^{+9}$ and $\log M_{\text{vir}} \sim 13.1 \pm 0.1M_{\odot}$, with errors including the variance of the assumed β profiles. In both these strongly radial models, the velocity dispersion bends quite significantly outside the last dispersion bin, which is a prediction that should be tested with more extended data.

We thus find that the impact of the outlier ambiguity is confined to the anisotropy conclusions, with highly radial halo orbits suggested by the kurtosis but hardly matched by the dispersion profile which is flatter when the two uncertain outliers are included. The mass profile inferences are presumably unaffected because of the pinch-point phenomenon, whereby the projected dispersion is only weakly dependent on anisotropy in certain regions of the galaxy. Further observations of PNe at larger radii (see e.g. Arnaboldi et al. 2004), particularly on the West side of the galaxy, could clarify the situation by more strongly constraining the dispersion and kurtosis profiles past the pinch point.

REFERENCES

- An, J. H., & Evans, N. W., 2006, *AJ*, 131, 782
 Arnaboldi, M. et al., 1996, *ApJ*, 472, 145
 Arnaboldi, M., Gerhard, O., Aguerra, J. A. L., Freeman, K. C., Napolitano, N. R., Okamura, S., & Yasuda, N. 2004, *ApJ*, 614, L33
 Auger, M. W., Treu, T., Bolton, A. S., Gavazzi, R., Koopmans, L. V. E., Marshall, P. J., Moustakas, L. A., & Bures, S. 2010, *ApJ*, submitted, arXiv:1007.2880
 Begeman, K. G., Broeils, A. H., & Sanders, R. H. 1991, *MNRAS*, 249, 523
 Bender, R., Saglia, R. P., & Gerhard, O. E., 1994, *MNRAS*, 269, 785 (B+94)
 Bergond, G., Zepf, S. E., Romanowsky, A. J., Sharples, R. M., & Rhode, K. L., 2006, *A&A*, 448, 155
 Bertin, G., et al. 1994, *A&A*, 292, 381
 Binney, J., & Tremaine, S. 1987, Princeton, NJ, Princeton University Press, 1987, 747 p.
 Blakeslee, J. P., Lucey, J. R., Barris, B. J., Hudson, M. J., & Tonry, J. L. 2001, *MNRAS*, 327, 1004
 Blumenthal, G. R., Faber, S. M., Flores, R., & Primack, J. R. 1986, *ApJ*, 301, 27
 Bower, G. A., et al. 1998, *ApJ*, 492, L111
 Bullock, J. S., Kolatt, T. S., Sigad, Y., Somerville, R. S., Kravtsov, A. V., Klypin, A. A., Primack, J. R., & Dekel, A., 2001, *MNRAS*, 321, 559
 Buote, D. A., Gastaldello, F., Humphrey, P. J., Zappacosta, L., Bullock, J. S., Brighenti, F., & Mathews, W. G., 2007, *ApJ*, 664, 123
 Calura, F., Jimenez, R., Panter, B., Matteucci, F., Heavens, A. F., 2008, *ApJ*, 682, 252
 Capaccioli, M., Caon, N., & D’Onofrio, M., 1992, *MNRAS*, 259, 323
 Cappellari, M., et al., 2006, *MNRAS*, 366, 1126 (C+06)
 Cappellari, M., et al., 2007, *MNRAS*, 379, 418
 Chanamé, J., Kleyana, J., & van der Marel, R. 2008, *ApJ*, 682, 841
 Chen, D.-M., & McGaugh, S. 2008, arXiv:0808.0225
 Cimatti A., Daddi E., Renzini A., 2006, *A&A* 453, L29
 Coccato, L., et al. 2009, *MNRAS*, 394, 1249 (C+09)
 Das, P., Gerhard, O., Churazov, E., & Zhuravleva, I. 2010, *MNRAS*, in press, [preprint:arXiv:1007.5322]
 Dejonghe, H., 1986, *PhR*, 133, 217
 Dekel, A., Stoehr, F., Mamon, G. A., Cox, T. J., Novak, G. S., & Primack, J. R., 2005, *Nat*, 437, 707 (D+05)
 De Lorenzi, F., Gerhard, O., Saglia, R. P., Sambhus, N., Debattista, V. P., Pannella, M., & Méndez, R. H., 2008a, *MNRAS*, 385, 1729
 De Lorenzi, F., et al. 2009, *MNRAS*, 395, 76 (DL+09)
 de Vaucouleurs, G., de Vaucouleurs, A., Corwin, H. G., Jr., Buta, R. J., Paturel, G., & Fouque, P., 1991, Volume 1-3, XII, 2069 pp. 7 figs.. Springer-Verlag Berlin Heidelberg New York
 Douglas, N. G., et al. 2002, *PASP*, 114, 1234
 Douglas, N. G., et al. 2007, *ApJ*, 664, 257 (D+07)
 Duffy, A. R., Schaye, J., Kay, S. T., Dalla Vecchia, C., Battye, R. A., & Booth, C. M. 2010, *MNRAS*, 405, 2161
 Emsellem, E., et al., 2007, *MNRAS*, 379, 401
 Faber, S. M. & Jackson, R.E. 1976, *ApJ*, 204, 668F
 Fall, S. M., & Efstathiou, G., 1980, *MNRAS*, 193, 189
 Finoguenov, A., & Jones, C. 2001, *ApJL*, 547, L107
 Finoguenov, A., Ruszkowski, M., Jones, C., Brüggner, M., Vikhlinin, A., & Mandel, E. 2008, *ApJ*, 686, 911
 Forestell, A. D., & Gebhardt, K. 2010, *ApJ*, 716, 370
 Gentile, G., Burkert, A., Salucci, P., Klein, U., & Walter, F., 2005, *ApJ*, 634, L145
 Gerhard, O., Kronawitter, A., Saglia, R. P., & Bender, R., 2001, *AJ*, 121, 1936
 Gerhard, O. E. 1993, *MNRAS*, 265, 213
 Gilmore, G., Wilkinson, M. I., Wyse, R. F. G., Kleyana, J. T., Koch, A., Evans, N. W., & Grebel, E. K., 2007, *ApJ*, 663, 948
 Gnedin, O. Y., Kravtsov, A. V., Klypin, A. A., & Nagai, D., 2004, *ApJ*, 616, 16
 Governato, F., et al. 2010, *Nature*, 463, 203
 Graves G. J., Faber S. M., Schiavon R. P., Yan R., 2007, 2007, *ApJ*, 671, 243
 Henon, M., 1973, *A&A*, 24, 229
 Herrmann, K. A., & Ciardullo, R. 2009, *ApJ*, 705, 1686
 Hinshaw, G., et al. 2009, *ApJS*, 180, 225
 Hopkins, P. F., Lauer, T. R., Cox, T. J., Hernquist, L., & Kormendy, J. 2009, *ApJS*, 181, 486
 Humphrey, P. J., Buote, D. A., Gastaldello, F., Zappacosta, L., Bullock, J. S., Brighenti, F., & Mathews, W. G., 2006, *ApJ*, 646, 899
 Hwang, H. S., et al. 2008, *ApJ*, 674, 869

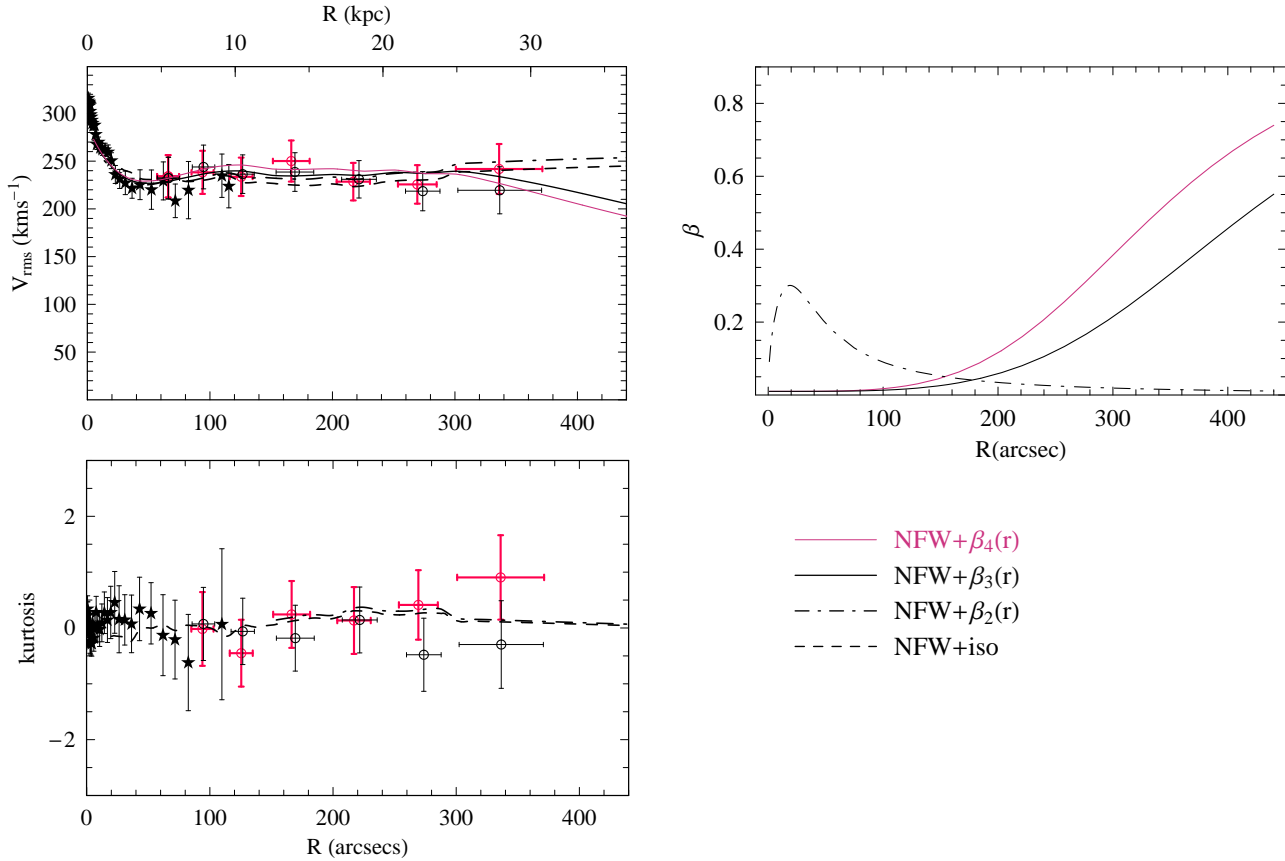


Figure A2. Effect of the outliers selection. *Top:* the velocity dispersion profile of the outliers selection with the friendless algorithm, adopted in the paper (black) is compared with the dispersion obtained by including the two uncertain outliers along the 3σ borderline (red). *Bottom:* the same for the kurtosis profile. Overplotted there are the isotropic model obtained for both profiles, and a best fit model with a steeply increasing $\beta(r)$ profile as suggested by the kurtosis including the two uncertain outliers, as in the top-right panel. Models are as in the legend. See text for details.

Jaffe, W., Ford, H. C., O’Connell, R. W., van den Bosch, F. C., & Ferrarese, L. 1994, *AJ*, 108, 1567
 Janowiecki, S., Mihos, J. C., Harding, P., Feldmeier, J. J., Rudick, C., & Morrison, H. 2010, *ApJ*, 715, 972
 Jensen, J. B., Tonry, J. L., Barris, B. J., Thompson, R. I., Liu, M. C., Rieke, M. J., Ajhar, E. A., & Blakeslee, J. P., 2003, *ApJ*, 583, 712
 Joanes, D. N. & Gill, C. A. 1998, *The Statistician*, 47, 183
 Johansson, P. H., Naab, T., & Ostriker, J. P. 2009, *ApJ*, 697, L38
 Johnson, R., Chakrabarty, D., O’Sullivan, E., & Raychaudhury, S. 2009, *ApJ*, 706, 980
 Komatsu, E., et al. 2009, *ApJS*, 180, 330
 Kormendy, J., & Bender, R. 1996, *ApJ*, 464, L119
 Kormendy, J., Fisher, D. B., Cornell, M. E., & Bender, R. 2009, *ApJS*, 182, 216
 Krajnović, D., et al. 2008, *MNRAS*, 390, 93
 Kronawitter, A., Saglia, R. P., Gerhard, O., & Bender, R., 2000, *A&As*, 144, 53 (K+00)
 Kroupa, P., 2001, *MNRAS*, 322, 231
 Kuzio de Naray, R., McGaugh, S. S., & de Blok, W. J. G. 2008, *ApJ*, 676, 920
 Lackner, C. N., & Ostriker, J. P. 2010, *ApJ*, 712, 88
 Laing, R. A., & Bridle, A. H. 1987, *MNRAS*, 228, 557

Lokas, E. L., 2002, *MNRAS*, 333, 697
 Lokas, E. L., & Mamon, G. A., 2003, *MNRAS*, 343, 401
 Macciò, A. V., Dutton, A. A., & van den Bosch, F. C., 2008, *MNRAS*, 391, 1940
 Magorrian, J., & Ballantyne, D., 2001, *MNRAS*, 322, 702
 Mamon, G. A., & Lokas, E. L., 2005, *MNRAS*, 363, 705 (ML05)
 McGaugh, S. S., de Blok, W. J. G., Schombert, J. M., Kuzio de Naray, R., & Kim, J. H., 2007, *ApJ*, 659, 149
 Méndez, R. H., Teodorescu, A. M., & Kudritzki, R.-P. 2009, *ApJS*, 175, 522
 Méndez, R. H., Teodorescu, A. M., Kudritzki, R.-P., & Burkert, A. 2009, *ApJ*, 691, 228
 Merrett, H. R., et al. 2003, *MNRAS*, 346, L62
 Merrett, H. R., et al. 2006, *MNRAS*, 369, 120
 Naab, T., Johansson, P. H., Ostriker, J. P., & Efstathiou, G., 2007, *ApJ*, 658, 710
 Napolitano, N. R., Arnaboldi, M., Freeman, K. C., & Capaccioli, M., 2001, *A&A*, 377, 784
 Napolitano, N.R., Arnaboldi, M., Capaccioli, M., 2002, *A&A*, 383, 791
 Napolitano, N. R., et al. 2005, *MNRAS*, 357, 691 (N+05)
 Napolitano, N. R., et al. 2008, *IAU Symposium*, 244, 289
 Napolitano, N. R., et al. 2009, *MNRAS*, 393, 329 (N+09)

- Napolitano, N. R., Romanowsky, A. J., & Tortora, C. 2010, *MNRAS*, 405, 2351
- Nelan J. E., Smith R. J., Hudson M. J., Wegner G. A., Lucey J. R., Moore S. A. W., Quinney S. J., & Suntzeff N. B. 2005, *ApJ*, 632, 137
- Noordermeer, E., et al., 2008, *MNRAS*, 384, 943
- Oñorbe, J., Domínguez-Tenreiro, R., Sáiz, A., & Serna, A., 2007, *MNRAS*, 376, 39
- O'Sullivan, E., & Ponman, T. J., 2004a, *MNRAS*, 349, 535
- O'Sullivan, E., & Ponman, T. J. 2004b, *MNRAS*, 354, 935
- Pannella M., Hopp U., Saglia R. P., Bender R., Drory N., Salvato M., Gabasch A., Feulner G., 2006, *ApJ*, 639, L1
- Paolillo, M., Fabbiano, G., Peres, G., & Kim, D.-W., 2003, *ApJ*, 586, 850
- Paturel, G., Petit, C., Prugniel, P., Theureau, G., Rousseau, J., Brouty, M., Dubois, P., & Cambrésy, L. 2003, *A&A*, 412, 45
- Pedrosa, S., Tissera, P. B., & Scannapieco, C. 2010, *MNRAS*, 402, 776
- Pellegrini, S., & Ciotti, L., 2006, *MNRAS*, 370, 1797
- Pellegrini, S., Baldi, A., Kim, D. W., Fabbiano, G., Soria, R., Siemiginowska, A., & Elvis, M., 2007, *ApJ*, 667, 731
- Peng, E. W., Ford, H. C., & Freeman, K. C., 2004, *ApJ*, 602, 685
- Persic, M., Salucci, P., & Stel, F., 1996, *MNRAS*, 281, 27
- Pu, S. B., Saglia, R. P., Fabricius, M. H., Thomas, J., Bender, R., & Han, Z. 2010, *A&A*, 516, A4
- Rodionov, S. A., & Athanassoula, E. 2010, *MNRAS*, in press, arXiv:1007.5200
- Romanowsky, A. J., Douglas, N. G., Arnaboldi, M., Kuijken, K., Merrifield, M. R., Napolitano, N. R., Capaccioli, M., & Freeman, K. C., 2003, *Science*, 301, 1696 (R+03)
- Romanowsky, A. J., Strader, J., Spitler, L. R., Johnson, R., Brodie, J. P., Forbes, D. A., & Ponman, T. 2009, *AJ*, 137, 4956
- Salucci, P., Lapi, A., Tonini, C., Gentile, G., Yegorova, I., & Klein, U., 2007, *MNRAS*, 378, 41
- Salpeter, E. E. 1955, *ApJ*, 121, 161
- Schlegel, D. J., Finkbeiner, D. P., & Davis, M., 1998, *ApJ*, 500, 525
- Schuberth, Y., Richtler, T., Hilker, M., Dirsch, B., Bassino, L. P., Romanowsky, A. J., & Infante, L. 2010, *A&A*, 513, A52
- Schulz, A. E., Mandelbaum, R., & Padmanabhan, N. 2010, *MNRAS*, submitted, arXiv:0911.2260
- Sersic, J. L. 1968, *Atlas de galaxias australes* (Cordoba, Argentina: Observatorio Astronomico, 1968)
- Shapiro, K. L., Cappellari, M., de Zeeuw, T., McDermid, R. M., Gebhardt, K., van den Bosch, R. C. E., & Statler, T. S., 2006, *MNRAS*, 370, 559
- Shen, S., Mo, H.J., White, S.D.M., Blanton, M.R., Kauffmann, G., Voges, W., Brinkmann, J., Csabai, I. 2003, *MNRAS*, 343, 978
- Shen, J., & Gebhardt, K. 2010, *ApJ*, 711, 484
- Spano, M., Marcelin, M., Amram, P., Carignan, C., Epinat, B., & Hernandez, O., 2008, *MNRAS*, 383, 297
- Teodorescu, A. M., Méndez, R. H., Bernardi, F., Riffeser, A., & Kudritzki, R. P. 2010, *ApJ*, 721, 369
- Thomas, D., Maraston, C., Bender, R. & Mendes de Oliveira, C. 2005, *ApJ*, 621, 673
- Thomas, J., Saglia, R. P., Bender, R., Thomas, D., Gebhardt, K., Magorrian, J., Corsini, E. M., & Wegner, G., 2007, *MNRAS*, 382, 657
- Tiret, O., Combes, F., Angus, G. W., Famaey, B., & Zhao, H. S., 2007, *A&A*, 476, L1
- Tissera, P. B., White, S. D. M., Pedrosa, S., & Scannapieco, C. 2010, *MNRAS*, 406, 922
- Tonry, J. L., Dressler, A., Blakeslee, J. P., Ajhar, E. A., Fletcher, A. B., Luppino, G. A., Metzger, M. R., & Moore, C. B., 2001, *ApJ*, 546, 681
- Tortora, C., Napolitano, N. R., Romanowsky, A. J., Capaccioli, M., & Covone, G. 2009, *MNRAS*, 396, 1132
- Tortora, C., Napolitano, N. R., Cardone, V. F., Capaccioli, M., Jetzer, P., & Molinaro, R. 2010a, *MNRAS*, 407, 144
- Tortora, C., Napolitano, N. R., Romanowsky, A. J., & Jetzer, P. 2010b, *ApJ*, 721, L1
- Trujillo-Gómez, S., Klypin, A., Primack, J., & Romanowsky, A. J. 2010, *ApJ*, submitted, arXiv:1005.1289
- Wilkinson, M. I., & Evans, N. W., 1999, *MNRAS*, 310, 645
- van der Marel, R. P., & Franx, M., 1993, *ApJ*, 407, 525
- van der Marel, R. P. 1994, *MNRAS*, 270, 271
- Weijmans, A.-M., Krajnović, D., van de Ven, G., Oosterloo, T. A., Morganti, R., & de Zeeuw, P. T., 2008, *MNRAS*, 383, 1343
- Weijmans, A.-M., et al. 2009, *MNRAS*, 398, 561
- Wolf, J., Martinez, G. D., Bullock, J. S., Kaplinghat, M., Geha, M., Muñoz, R. R., Simon, J. D., & Avedo, F. F. 2010, *MNRAS*, 406, 1220
- Woodley, K. A., Gómez, M., Harris, W. E., Geisler, D., & Harris, G. L. H. 2010, *AJ*, 139, 1871